Ye Xinxin (Orcid ID: 0000-0001-8558-1294)
Lauvaux Thomas (Orcid ID: 0000-0002-7697-742X)
Kort Eric, A. (Orcid ID: 0000-0003-4940-7541)
Oda Tomohiro (Orcid ID: 0000-0002-8328-3020)
Feng Sha (Orcid ID: 0000-0002-2376-0868)
Lin John, C. (Orcid ID: 0000-0003-2794-184X)
Yang Emily, G. (Orcid ID: 0000-0001-5195-9279)
Wu Dien (Orcid ID: 0000-0002-2915-5335)

Confidential manuscript submitted to Journal of Geophysical Research: Atmosphere

Constraining fossil fuel CO_2 emissions from urban area using OCO-2 observations of total column CO_2

Xinxin Ye[1*], Thomas Lauvaux[1†], Eric A. Kort[2], Tomohiro Oda[3,4], Sha Feng[1], John C. Lin[5], Emily G. Yang[2], Dien Wu[5]

[1]Department of Meteorology and Atmospheric Science, The Pennsylvania State University, University Park, PA 16803, USA, [2]Department of Climate and Space Sciences and Engineering, University of Michigan, Ann Arbor, MI 48109, USA, [3]Global Modeling and Assimilation Office, NASA Goddard Space Flight Center, Greenbelt, MD 20706, USA, [4]Goddard Earth Sciences Technology and Research, Universities Space Research Association, Columbia, MD 21046, USA, [5]Department of Atmospheric Sciences, University of Utah, Salt Lake City, UT 84132, USA

Corresponding author: Xinxin Ye (xuy112@psu.edu)
*Now at Department of Atmospheric and Oceanic Sciences, University of California, Los Angeles, Los Angeles, CA 90095, USA
†Now at Laboratoire des Sciences du Climat et de l'Environnement, CEA, CNRS, UVSQ/IPSL, Université Paris-Saclay, Orme des Merisiers, Gif-sur-Yvette cedex 91191, France

Key Points:

- Inversion method is utilized to constrain whole-city fossil fuel emissions with measurement and transport model errors considered
- Potential of incorporating multiple tracks to obtain regular emission estimates is evaluated by pseudo data experiments
- Significant contribution of the biospheric fluxes variability to local X_{CO2} variation is demonstrated

Abstract

Satellite observations of the total column dry-air CO_2 (X_{CO2}) are expected to support the quantification and monitoring of fossil fuel CO_2 ($ffCO_2$) emissions from urban areas. We evaluate the utility of the Orbiting Carbon Observatory 2 (OCO-2) X_{CO2} retrievals to optimize whole-city emissions, using a Bayesian inversion system and high-resolution transport modeling. The uncertainties of constrained emissions related to transport model, satellite measurements, and local biospheric fluxes are quantified. For the first two uncertainty sources, we examine cities of different landscapes: "plume city" located in relatively flat terrain, represented by Riyadh and Cairo; "basin city" located in basin terrain, represented by Los Angeles (LA). The retrieved scaling factors of emissions and their uncertainties show prominent variabilities from track to track, due to the varying meteorological conditions and relative locations of the tracks transecting plumes. To explore the performance of multiple tracks in retrieving emissions, pseudo data experiments are carried out. The estimated least number of tracks required to constrain the total emissions for Riyadh (<10% uncertainty), Cairo (<10%), and LA (<5%) are 5, 8, and 7, respectively. Additionally, to evaluate the impact of biospheric fluxes on derivation of the ffX_{CO2} enhancements, we conduct simulations for Pearl River Delta metropolitan area. Significant fractions of local X_{CO2} enhancements associated with local biospheric X_{CO2} variations are shown, which potentially lead to biased estimates of $ffCO_2$ emissions. We demonstrate that satellite measurements can be used to improve urban $ffCO_2$ emissions with a sufficient amount of measurements and appropriate representations of the uncertainty components.

1 Introduction

The global atmospheric CO_2 concentration has increased by more than 40% since the pre-industrial era to more than 400 ppm in recent years and remains the main driver to current and future climate changes (Le Quéré et al., 2018). The increase in CO_2 concentration predominantly originates from anthropogenic CO_2 emissions by combustion of fossil fuels such as coal, petroleum, and natural gas (Andres et al., 2012; Ciais et al., 2013; Rotty, 1983). In order to foster the mitigation and management of anthropogenic CO_2 emissions, the international community has pursued treaties and agreements in the recent decades, such as the Kyoto Protocol (United Nations, 1998) and the Paris Agreement (UNFCCC, 2015).

A large percentage of the anthropogenic CO_2 is emitted from urban areas. About 40% as estimated by production-based figures (i.e. adding up emissions from entities located within cities), and as high as 60-70% with a consumption-based method (i.e. adding up emissions resulting from the production of all goods consumed by urban residents) (International Energy Agency, 2008; UN-Habitat, 2011; Satterthwaite, 2008). Given their significant contributions to fossil fuel CO_2 ($ffCO_2$), cities can perform as leading entities in implementing emission reduction plans. Comprehensive, accurate, and comparable emission quantifications are crucial for transparent monitoring of $ffCO_2$ emissions from urban areas and implementing effective mitigation schemes (Duren and Miller, 2012; Gurney et al., 2015; Pacala et al., 2010).

Emission inventory compilations with two methods referred to as “bottom-up” and “downscaling” are generally used to quantify $ffCO_2$ emissions. However, urban emissions usually bear large uncertainties, due to the missing socio-economic information and inaccurate emission conversion factors, which are critical elements affecting the quality of emission inventories at the urban scale (Gately and Hutyra, 2017). For example, urban energy consumption and industrial activity data needed for “bottom-up” method are reported on a voluntary basis, or under climate action activities in only a few cities, e.g., those participating the Global Covenant of Mayors (http://www.globalcovenantofmayors.org/), and are usually spatially inexplicit, incomplete and

unverified (Hutyra et al., 2014). Similarly, for inventories developed by disaggregating ("downscaling") national or regional emissions at fine scales, the uncertainty is large at high spatial and temporal resolutions caused by the disaggregation methods (Janssens-Maenhout et al., 2012; Kurokawa et al., 2013; Oda and Maksyutov, 2011), resulting in significant discrepancies among different emission inventories (Ackerman and Sundquist, 2008; Denier van der Gon et al., 2012; Gurney et al., 2012, 2019; Hogue et al., 2016; Oda et al., 2018; Oda and Maksyutov, 2011; Turnbull et al., 2011a). The two-sigma uncertainties of national annual $ffCO_2$ emissions are estimated to be 2~4% for countries with well-developed energy statistics and inventories (Rypdal and Winiwarter, 2001), and are at a possible order of 10% for countries with less well-developed energy data systems (IPCC, 2006). Nevertheless, urban-scale emission inventories can exhibit large differences (50-250%) compared to other downscaled datasets at local scales (Gately and Hutyra, 2017). The large uncertainties in $ffCO_2$ emissions not only impose difficulties on evaluating the effects of emission reduction strategies, but also would lead to significant biases in the regional carbon budget estimations (Corbin et al., 2010). It is reported by ESA (2015) that, accuracies of inferred emissions in the order of 10% of the total would be needed for providing constraints that allows emission inventories to be evaluated at the time of an overpass. For cities that do not have inventories, an accuracy of 20% is already an important gain in information.

Atmospheric observations-based methods are becoming important ways to objectively obtain $ffCO_2$ emission estimates, allowing existing emission inventories to be improved. Some attempts have been made to derive local-scale emissions for the urban areas by utilizing the inverse modeling method (Bousquet, 2000; Ciais et al., 2010) with ground-based observations (Bréon et al., 2015; Lauvaux et al., 2016; McKain et al., 2012; Staufer et al., 2016; Wunch et al., 2009), or by the mass-balance approach with aircraft measurements (Cambaliza et al., 2014). However, one of the key limitations of these approaches is the unavailability of direct, continuous, and high-frequency atmospheric CO_2 measurements representing CO_2 enhancement in urban areas (Bréon et al., 2015), as only a handful of cities, mostly in Europe and North America, are instrumented with networks of CO_2 sensors (Bréon et al., 2015; Davis et al., 2017; McKain et al., 2012; Miles et al., 2017; Verhulst et al., 2017).

In recent decades, space-based satellite measurements of column-averaged CO_2 dry air mole fractions (X_{CO2}) have been highly recommended for quantification and monitoring of urban $ffCO_2$ emissions, especially for cities where ground-based observations are sparse or unavailable (Duren and Miller, 2012; Kort et al., 2012; McKain et al., 2012; Schneising et al., 2013). Initial attempts have been made to relate satellite X_{CO2} measurements to $ffCO_2$. Based on the retrievals from Scanning Imaging Absorption Spectrometer for Atmospheric Chartography (SCIAMACHY) on ENVISAT (2002-2012) (Bovensmann et al., 1999; Buchwitz et al., 2005), regional X_{CO2} enhancements over the industrial areas in Germany were revealed to be correlated with yearly increase of anthropogenic CO_2 emissions (Schneising et al., 2008, 2013). In addition, with the launch of Greenhouse gases Observing SATellite (GOSAT) in 2009 (Kuze et al., 2009; Morino et al., 2011), discernible X_{CO2} contrasts between the emission and background regions (Janardanan et al., 2016; Keppel-Aleks et al., 2013), as well as local X_{CO2} enhancements over megacities (Kort et al., 2012) have been reported. However, due to coarse spatial resolution (~ 60 km × 30 km) and relatively low sensitivity (4~8 ppm) of the SCIAMACHY instrument, applications of its data are limited to large and intense emission regions. For the GOSAT instrument, the major limitation is its low sounding density, with a single 85-km^2 measurement per 250 km, resulting in fewer than 1000 cloud-free soundings each day (Eldering et al., 2017b). Hence, these datasets are insufficient to enable accurate assessment of $ffCO_2$ urban emissions at high spatial and temporal resolutions.

NASA's Orbiting Carbon Observatory 2 (OCO-2) satellite mission (Crisp, 2008; Crisp et al., 2004) has been providing continuous and global retrievals of X_{CO2} since September 2014 (Crisp, 2015). Although the OCO-2 mission is primarily developed for assessing regional carbon sources and sinks, its unique characteristics allow for detection of X_{CO2} enhancements over cities at fine scales. The OCO-2 measurements have a higher spatial resolution than GOSAT and SCIAMACHY and collects more data per day. In particular, the small nadir footprint (~1.29 km × 2.25 km) helps to maximize the detectability of local emissions and increase the probability of cloud-free observations in the presence of patchy clouds. In addition, the high spectral resolution of OCO-2 enables high precision of X_{CO2} with single sounding random errors of 0.5~1 ppm (Eldering et al., 2017a), which will greatly help to

detect the small anthropogenic X_{CO2} signals from the large background driven by biospheric sources and sinks and large scale atmospheric transport (Keppel-Aleks et al., 2013; Turnbull et al., 2016). There have been some studies to examine X_{CO2} imprints linked to anthropogenic emissions with the OCO-2 data. For example, spatial enhancements have been reported over the Northern Hemisphere regionally (Hakkarainen et al., 2016) and across the Los Angeles basin (Schwandner et al., 2017). For local-scale emissions and point sources, atmospheric transport modeling approach is applied to disentangle $ffCO_2$ emissions from background. Wu et al. (2018) developed a Lagrangian model to interpret the X_{CO2} retrievals and constrain emissions from some cities in the Middle East. Nassar et al. (2017) presented the capability of quantifying $ffCO_2$ emissions from individual power plants by utilizing a Gaussian plume model.

Although the abovementioned studies have demonstrated the utility of OCO-2 X_{CO2} on revealing $ffCO_2$ emissions, the emission estimation has not been carried out with high-spatial-resolution forward transport modeling so far, which has an advantage in capturing the fine-scale structure of $ffCO_2$ plume. Meanwhile, it is essential to evaluate the uncertainty in emission estimate related to atmospheric transport model error with the high-resolution plume simulations, which has been identified as a major source of uncertainty in inverse modeling (Gerbig et al., 2003; Houweling et al., 2010; Lauvaux et al., 2012; Lauvaux and Davis, 2014; Lin and Gerbig, 2005; Miller et al., 2015; Pacala et al., 2010). Additionally, the uncertainty in biosphere X_{CO2} at local scale increases the difficulty of unambiguously disentangling fossil-fuel emission signals in X_{CO2} from the observations for cities in vegetated areas, which has not been evaluated in respect of space-based total column observations.

The previous studies were focused on cases using individual OCO-2 tracks. However, from the perspective of tracking $ffCO_2$ emissions for global cities on a regular basis, the potential of OCO-2 retrievals has yet to be investigated, which will be helpful to provide regular and policy-relevant references in support to improving the emission reduction strategies. Given current limitations in remote sensing that create a trade-off in sampling coverage and measurement precision, OCO-2 was designed as a sampling mission to provide measurements at high precision, but only samples a small

fraction of the globe each day (Eldering et al., 2017b), with a narrow swath (~10.3 km) and a long revisit cycle (~16 days). These features enable a small percentage of local emissions to be detected in each cycle (Pacala et al., 2010). Moreover, because the OCO-2 sampling locations vary among different observation modes (nadir, glint, and target), and the atmospheric transport condition changes, overpasses that happen to detect fossil-fuel X_{CO2} enhancements across a certain city are limited. For the cities examined in this work, about 5-15% of nearby OCO-2 tracks show detectable urban plumes, based on 15 months of OCO-2 data (September 2014 to November 2015). Hence, it would be still difficult to regularly monitor emissions by using individual overpasses. Despite these limitations, there is a potential to constrain fossil fuel emissions regularly by utilizing data collected along multiple tracks over one or more revisit cycle(s), which could enable tracking emission variations, although at a lower temporal resolution.

In this paper, we present the utility of OCO-2 X_{CO2} data to constrain $ffCO_2$ emission estimations for urban areas. Several sources of uncertainty in emission estimate are evaluated, including the transport model errors, measurement errors, and variations in local biospheric carbon fluxes. High-resolution forward simulations are performed using the Weather Research and Forecast (WRF) model, which is capable of capture fine-scale variability in X_{CO2} distributions caused by transport and emission processes at urban scales. We first evaluate the emission estimate uncertainty related to transport model errors and measurement errors for three selected cities with different topographic influences and negligible impact of variations in local biospheric fluxes, i.e. Riyadh and Cairo, classified as “plume cities” located in relatively flat terrain, and Los Angeles as a “basin city”. Based on these simulations, we carried out Observing System Simulation Experiments (OSSEs) to evaluate the potential of tracking urban emissions regularly by utilizing X_{CO2} data from multiple OCO-2 tracks. We also evaluated the uncertainty induced by local biospheric fluxes variability for the Pearl River Delta metropolitan area. We discuss additional uncertainty sources in the inverse emission estimates, e.g. the prior emission error correlations and the daytime-only sampling, and conclude with the implications for utilizing future satellite observations to monitor urban emissions.

2 Data and Method

2.1 OCO-2 X_{CO2} observations

The OCO-2 Lite files (version 7r) from September 2014 to November 2015 are used in this study (obtained online at https://co2.jpl.nasa.gov). The OCO-2 satellite operates in a sun-synchronous polar orbit at the altitude of about 705 km and crosses the equator nominally at 13:36 LT (Local Time). It provides high-resolution spectroscopic measurements at eight adjacent 2.25 km long footprints within a narrow swath every 0.333 s, with a cross-track resolution of 0.1~1.3 km (Crisp, 2008; Eldering et al., 2017a). The X_{CO2} data are retrieved from the spectroscopic observations of reflected sunlight in near-infrared CO_2 and O_2 bands near midday, using the Atmospheric CO_2 Observations from Space (ACOS) algorithm (O'Dell et al., 2012). We used the bias-corrected X_{CO2} data and filter them with "xco2_quality_flag" (QF) equals to zero, which is an indicator of data passing the internal quality check. The bias correction and data quality assessment have been detailed in the OCO-2 documentation (Mandrake et al., 2015). In addition, we analyzed each individual track over the selected cities for possible interferences by complex terrain, aerosols, and clouds. Some tracks were excluded due to contaminations by aerosols or clouds, as confirmed with the Cloud-Aerosol Lidar with Orthogonal Polarization (CALIOP) data (Winker, 2016). The OCO-2 X_{CO2} data are averaged over time windows of 1 s, consisting of 24 consecutive soundings (at most) representing ~10.32 km (cross track) × 6.75 km (along track) in area. Note that we only derive 1-s average X_{CO2} when there are at least 5 soundings (at most 24) in that time window passing the data selection criteria.

The measurement error of each X_{CO2} sounding consists of two parts: a random error related to noise, and a systematic error that is in principle bounded by the calculated interference error owing primarily to aerosol optical depth, surface albedo, and surface pressure (Boxe et al., 2010). For the random error, the OCO-2 data products include an estimate of the uncertainty on X_{CO2}, which is generally smaller over water than the land surface, and larger at the extreme latitudes (Eldering et al., 2017a). However, this estimation is a lower bound (Connor et al., 2016). Worden et al. (2017) evaluated the OCO-2 uncertainty by examining the X_{CO2} variability within small neighborhoods of ~100 km × 10.5 km, in

which natural CO_2 variability is expected to be small. It is shown that the random error in the data product over land (~0.36 ppm) is smaller than the empirically derived X_{CO2} random error (~0.75 ppm) by a factor of approximately 2. Conservatively, we consider a random error for each X_{CO2} sounding with the standard deviation of 1 ppm, which leads to 0.20~0.45 ppm for the 1-s average data calculated with 5~24 soundings.

For the systematic error, as we used the bias-corrected data, some biases have been removed, e.g. systematic footprint-to-footprint differences, mode-to-mode differences, and systematic differences that appear to be correlated to other retrieval variables (Mandrake et al., 2015). However, as validated using the Total Carbon Column Observing Network (TCCON) X_{CO2} measurements by Wunch et al., (2017), residual biases remain in the OCO-2 retrievals after bias correction, with the absolute median differences <0.4 ppm and RMS differences <1.5 ppm. These biases appear to depend on latitude, surface properties, and scattering by aerosols. We note that for OCO-2 nadir and glint modes, these biases are evaluated using aggregated X_{CO2} data within a box centered around the TCCON station that spans 5° in latitude (~555 km) and 10° in longitude (~1100 km) on the same day as a TCCON measurement. As we examine the variability in X_{CO2} at a smaller spatial scale (~200-300 km, see Table 1 for the domain sizes), these biases in background can be removed when we extract local X_{CO2} enhancements associated with fossil fuel emissions (ffX_{CO2}) by subtracting the background X_{CO2}. Due to the lack of an accurate representation of aerosol contamination in the current retrieval algorithm, we assume that the effects of urban aerosols on X_{CO2} retrievals are negligible. Hence, the local ffX_{CO2} derived from OCO-2 observations are assumed to be unbiased in this paper. Details of the derivation of background X_{CO2} can be found in section 2.2.

2.2 Background X_{CO2}

We extract ffX_{CO2}, i.e. X_{CO2} enhancements caused by $ffCO_2$ emissions, by subtracting background X_{CO2} from the OCO-2 X_{CO2} retrievals. A typical method to derive $ffCO_2$ from in-situ CO_2 measurements is to calculate the difference between CO_2 at an upwind site and a downwind site (e.g. Bréon et al., 2015; Super et al., 2017; Lauvaux et al., 2016). The best application condition of this

constant background method is when the wind vector is aligned with the stations. Similarly, when the wind is aligned with the orbit, we could get background X_{CO2} by averaging the measurements in the upwind region of a city. However, the alignment is very rare for OCO-2 (Nassar et al., 2017). In previous studies, a constant background is often used for X_{CO2} retrievals collected over a time period, which is calculated as the median X_{CO2} over a latitudinal band (Hakkarainen et al., 2016) or the average X_{CO2} in a "background area", e.g. the desert located close to Los Angeles (Kort et al., 2012). However, for a single overpass, a constant background would not represent the spatial variability of the background concentrations. Thus, for each single overpass across a city of interest, we derived a "background line", as shown with the black lines in Figs. 4, 5, and 7. The "background line" is derived by a two-step linear regression. We firstly decompose the X_{CO2} data into two parts, i.e. $X_{CO2}=X_{CO2\_}trend+X_{CO2\_}local$, where the $X_{CO2\_}trend$ is the non-local trend represented using a linear function: $X_{CO2\_}trend=a\cdot x+b$. Here x is latitude, a and b are the slope and interception derived by linear regression. With the standard deviation of $X_{CO2\_}local$ (σ_{local}) representing the local-scale variability, we filtered the X_{CO2} samples with $X_{CO2} < X_{CO2\_}trend + 0.5\sigma_{local}$. These filtered data are chosen as "background samples" (the black triangles in Figs. 4, 5, and 7), as they have lower spatial variability at local scales compared to the samples affected by urban $ffCO_2$ emissions. Then we recalculate the linear regression line, i.e. the "background line", based on the "background samples". This "background line" method allows considering the spatial trend in the background.

2.3 Cities of interest

Four cities/urban areas are selected in this work considering the availability of OCO-2 data, topography, and vegetation coverage to highlight different sources of uncertainty in the emission estimates. To explore the impact of transport model errors, three different cities are chosen according to the following criteria: i) distant isolation from other large anthropogenic emission sources nearby, ii) large fossil-fuel carbon emissions, iii) low cloud cover and relatively preferable data availability, and iv) weak contribution of biospheric signals. Cities are categorized into two different types based on the impact of local topography on dispersion: "plume cities" located in relatively flat terrain, and "basin

cities" located in complex terrain trapping the dispersion. In this paper, Riyadh, Saudi Arabia with a population of 6.2 million, and Cairo, Egypt with 18.4 million are chosen as typical "plume cities", which are characterized by ffX_{CO2} enhancements distributed as plumes. The Los Angeles metropolitan area (referred to as LA hereafter) with a population of more than 13 million is chosen as a characteristic "basin city". The LA basin presents large elevation gradients from the sea surface to the top of Mount Wilson to the north. The strong enhancements in X_{CO2} are mainly due to air masses trapped in the basin, which has been referred to as "urban dome" (Idso et al., 1998), albeit we do not adopt this terminology in this work due to the potential confusion with actual accumulation of CO_2.

To evaluate the impact of uncertainties in biospheric fluxes on the emission estimate, the Pearl River Delta (PRD) region of China is selected, where an agglomeration of several cities is located, including Guangzhou, Hong Kong, Shenzhen, Zhuhai, Dongguan, and Zhongshan. The PRD region is one of the largest metropolitan area in the world with about 45 million people. The cities are less vegetated compared to their surrounding area, leading to a distinctive contrast in the Net Ecosystem Exchange (NEE) in the urban area and surrounding rural area (see Fig. S2 and section 2.4.3).

2.4 Model setup

2.4.1 Atmospheric transport model

The spatial heterogeneity of emissions and intense point sources (e.g. power plants) lead to complex spatial structures of urban emissions, resulting in complex CO_2 plume combined with local atmospheric dynamics (e.g. Feng et al., 2016). In order to capture the fine-scale variations, we simulate the ffX_{CO2} using the Weather Research and Forecasting model (V3.6.1) with chemistry (WRF-Chem) (Grell et al., 2005; Skamarock et al., 2008), coupled to CO_2 emissions and biospheric fluxes using the passive tracer mode (Lauvaux et al., 2012). Model grids are configured with 51 vertical (eta) levels. The 6-hourly NCEP FNL (Final) Operational Global Analysis data on 0.5°×0.5° grids are used as the initial and boundary conditions of meteorological and land surface fields. The boundary condition of CO_2 concentration for the outermost is 390.0 ppm. The simulations are initiated every 4 days at 12:00

UTC with an integration time of 108 hours, including a spin-up time of 12 hours and producing hourly outputs.

One-way nested domains with resolutions of 27, 9, 3, and 1 km are used for Riyadh and Cairo, 36, 12, and 4 km for LA, and 36, 12, 4, and 1.333 km for the PRD region. The innermost domains and distributions of $ffCO_2$ emission for the selected cities are shown in Fig. S3. For Riyadh, Cairo, and PRD, the innermost domains are used as the domains of interest to filter the OCO-2 observations. Note that for LA, the domain of interest is set to 119.0° W~116.3°W, 32.2°N~35.7°N, which is smaller than the innermost domain, and the spatial resolution is coarser than others. As reported by Feng et al. (2016), the 1.3 km run does not show significant improvement compared to the 4 km run at the surface, even though it resolves the vertical gradient of horizontal winds and PBL better. Given that aggregated ffX_{CO2} along track is used to compute the scaling factor of a priori emissions, we compared the aggregated ffX_{CO2} using 4-km and 1.3-km runs, and they also present similar results owing to ffX_{CO2} mostly being trapped within the basin during daytime. Therefore, we used 4-km resolution for LA in this study.

A summary of the simulations performed in this study is shown in Table 1. The fossil-fuel CO_2 emission data and NEE data are detailed in sections 2.4.2 and 2.4.3. Note that the simulations for tracers imposed by NEE are only conducted for the PRD region. Moreover, an ensemble of modeling based on model physics parameterizations is deployed to represent the transport model errors in the simulated ffX_{CO2} over LA (see section 2.5.1).

2.4.2 Fossil-fuel CO_2 emissions

The Open-source Data Inventory for Atmospheric Carbon dioxide (ODIAC) version 2015a (Oda et al., 2017, 2018; Oda and Maksyutov, 2011, 2015) is used in this paper for emissions from each cities of interest. The ODIAC emission product provides 1 km ×1 km gridded global and monthly fossil fuel CO_2 emissions. It is developed based on country-level fossil fuel CO_2 emission estimates, fuel consumption statistics, satellite-observed nightlight data, and point source information (geographical

locations and emission intensities) from the CARbon Monitoring for Action (CARMA) power plant database (Oda et al., 2018). The global nightlight data were used as a geo-referenced, spatial proxy to determine the spatial extent of anthropogenic emissions from the line and diffused (area) sources (e.g. road traffic, residential or commercial fuel consumption). The ODIAC gridded emission fields defined on a global rectangular (latitude × longitude) coordinate are remapped to meet the grid resolutions for each simulation domain. Note that temporal variability of emissions at diurnal and weekly scales is not included in the modeling and the pseudo data experiments. We remapped the monthly emission distributions for the time periods investigated in our simulation. The $ffCO_2$ emission distributions are shown in Fig. S3. All $ffCO_2$ is released at the ground surface.

2.4.3 Biogenic CO_2 fluxes

The Net Ecosystem Exchange (NEE) fluxes in the PRD region are provided by the 15 different global Terrestrial Biogeochemical Models (0.5°×0.5°) in the Multi-scale Synthesis and Terrestrial Model Intercomparison Project (MsTMIP) (Huntzinger et al., 2013). In order to better characterize the diurnal variability and spatial distribution of biogenic fluxes, a 3-hourly dataset for global biogenic fluxes (Fisher et al., 2016) is used, which is temporally downscaled from the monthly global models. Furthermore, we spatially downscale the 3-hourly NEE from the original MsTMIP grid (0.5°×0.5°) (e.g. Fig. 1a) to the WRF domains (36-, 12-, 4-, and 1.333-km resolutions) using the Green Vegetation Fraction (GVF), with the assumption that vegetation productivity and respiration scales linearly with canopy coverage in each grid cell. We note that using this method, besides plant productivity and respiration, soil respiration is also downscaled by GVF, which could lead to some misrepresentation of soil respiration although the impact on the results would be small. The GVF is defined as the fraction of the grid cell for which midday downward solar insolation is intercepted by a photosynthetically active green canopy. A robust relationship between canopy cover and biomass was observed in Boston, which supports the use of GVF as a proxy for biomass, and hence as a scaling parameter for biogenic fluxes (Briber et al., 2013; Raciti et al., 2012). The NEE can be downscaled as follows:

$$E_{wrf,\,i,\,j} = (E_{blin,\,i,\,j} / GVF_{blin,\,i,\,j}) \times GVF_{wrf,\,i,\,j} \tag{2.1}$$

where the subscripts *i* and *j* represent the coordinates of a WRF grid cell, E_{wrf} the NEE at WRF grid (e.g. Fig. 1c), and E_{blin} the bilinear interpolated NEE from the original 0.5°×0.5° grids to WRF grid (e.g. Fig. 1b). GVF_{blin} is interpolated using MODIS climatological GVF (e.g. Fig. 1d) in the same way of deriving E_{blin} (e.g. Fig. 1c), ensuring the same spatial representativeness of GVF_{blin} and E_{blin}, and GVF_{wrf} (e.g. Fig. 1e) is the GVF projected to the WRF grid. The GVF data used in this study are based on MODIS climatological observations from 2001 to 2010, which is available in the geographic data since WRF v3.6. The uncertainties in biogenic X_{CO2} are represented by the spread of simulated biogenic X_{CO2} using the NEE from the 15 member models in MsTMIP.

2.5 Representation of transport model errors

The impact of transport model errors in wind speed and wind direction on the uncertainty of emission estimates is considered in the inversions. In this section, we introduce the methods to propagate the transport model errors to the modelled ffX_{CO2} fields across different types of cities. The method applied for plume city and basin city are explained in section 2.5.1 and 2.5.2, respectively.

2.5.1 Plume city: transformation of plumes

For a "plume city", the transport model errors are propagated by transformation of the modeled ffX_{CO2} plume. More detail of this method is included in the supporting information (Text S1.1). The errors for the "plume city" are assumed to be unbiased based on the previous study on Indianapolis (Deng et al., 2017). For a random error (θ) in wind direction, we rotate the simulated plume $\bar{c}(x, y, t)$ at a given time (t) by an angle θ about the emission center (x_0, y_0) to get $\bar{c_r}(x_r, y_r, t)$. Then the rotated plume is transformed to incorporate random wind speed error (ε) as:

$$\overline{c_{r\prime}}(x_{r\prime}, y_{r\prime}, t) = \bar{c_r}(x_r, y_r, t), \tag{2.2}$$

where

$$x_{r\prime} = \frac{\bar{u}+\varepsilon}{\bar{u}}(x_r - x_0) + x_0,\ y_{r\prime} = y_r,\ z_{r\prime} = z_r,\ \overline{c_{r\prime}} = \bar{c_r}\frac{\bar{u}}{\bar{u}+\varepsilon}. \tag{2.3}$$

Since the $ffCO_2$ is confined within the planetary boundary layer (PBL) and well mixed during the daytime, we used the domain average wind speed within the PBL and its typical error statistics for

$\bar{u}$ *and* ε. The errors are assumed to follow normal distributions of N(0, 1.0) (unit: ms^{-1}) for wind speed and N(0, 15) (unit: °) for wind direction, respectively. The selection of the error ranges are consistent with the model error statistics in the lower troposphere (< 2 km) from model evaluation studies, e.g. Indianapolis (Deng et al., 2017), Los Angeles (Feng et al., 2016), and more generally over the US Upper Midwest (Diaz-Isaac et al., 2018).

Examples of transformed plumes using this method are shown in Fig. 2 based on a simulated ffX_{CO2} plume over Riyadh at about 10:00 UTC 29 December 2014. The impacts of positive and negative wind speed errors are represented by transformation (Figs. 2b and 2c), rescaling the plume along the domain average wind direction. The impact of a wind direction error is represented by a rotation of the plume (Fig. 2d).

To obtain the transport model uncertainty in the modeled ffX_{CO2}, we transform the modeled plume by multiple times (here 10^4) with random wind speed and wind direction errors, and extract the uncertainty spread of ffX_{CO2} by using the 25^{th} and 75^{th} percentiles. The transformation method is a tradeoff between running a simplified model (e.g. a Gaussian plume model) and running an ensemble of simulations. With this method, we can retain the complexity of X_{CO2} plume structures while exploring the transport error impact at low computational costs. Note that this method is derived under the assumption of spatially uniform wind errors, which is generally valid within a few tens of kilometers from the emission center.

2.5.2 Basin city: model physics-based ensemble simulation

For Los Angeles, a typical basin city, the transport model errors are represented by an ensemble of WRF simulations with different PBL and urban canopy physics parameterizations, following Feng et al. (2016). This method is suitable for transport conditions with the dispersion of CO_2 trapped by local topography. Four different PBL parameterizations are used, i.e. the Mellor-Yamada-Nakanishi-Niino (MYNN) 2.5 (Nakanishi and Niino, 2004) scheme, the Mellor-Yamada-Jancic (MYJ) scheme (Janjić, 1994), and the Bougeault and Lacarrère (BouLac) (Bougeault and Lacarrere, 1989) scheme. For the land surface processes in urban canopy, the single-layer urban canopy model (UCM) (Kusaka and

Kimura, 2004) and the multi-layer Building Environment Parameterization (BEP) (Martilli et al., 2002) are used. The ensemble of simulations with different combinations of the model physics schemes (Table 2) can represent the model uncertainties in wind field, PBL structure, as well as PBL height.

In order to evaluate the performance of the ensemble on representing the model-observation mismatches, the modeling results of wind speed and wind direction are compared with surface wind observations. Surface observations of wind speed and wind direction at 43 synoptic weather stations located within the 4-km domain covering Los Angeles were used, derived from the global hourly Integrated Surface Data (ISD) and accessible at the National Centers for Environmental Information (NCEI) (https://gis.ncdc.noaa.gov/geoportal/catalog/search/resource/details.page?id=gov.noaa.ncdc:C00532).

For each observation time, the mean absolute error (MAE) of modeling result is calculated to evaluate the magnitude of the model error. We compared the ensemble spread presented by two approaches: 1) the standard deviation (STD) of the ensemble results, and 2) semi-full range of the ensemble results (half of the difference between the maximum and minimum values). As shown in Fig. 3, both of the approaches based on the simulation results of the 6 members exhibit a somewhat lower ensemble spread of wind speed compared to the observed MAE, suggesting an underestimation of the transport uncertainty (Figs. 3a and 3b). When taking the model results at ±1 h relative to the observation time into account (Figs. 3c and 3d with the ensemble size of 18 members), the ensemble spread is found to be enlarged, suggesting a better agreement with the observed MAE. The ensemble spreads for wind speed and wind direction both show better agreement with the MAE. It can also notable that the semi-full range yields a better representation of the model uncertainty compared to the STD (Figs. 3c and 3d). Hence, for LA we use the 18 ensemble members and the semi-full range to estimate transport model uncertainty spread in the simulated ffX_{CO2}.

For the systematic errors in the transport model, we compared the ensemble mean surface wind speed to the observations. The result shows a positive bias of 0.48 ms^{-1}. Similarly, Angevine et al. (2012) found a wind speed bias of 1.1±2.7 ms^{-1}. Feng et al. (2016) reported a slightly smaller bias of ~1.0 ms^{-1} for LA, and showed larger biases near mountainous sites owing to complex topography. We

note that the wind speed error is evaluated at surface in this work. The wind speed bias varies at different altitudes through the PBL, with usually larger value near the surface (Feng et al., 2016).

The wind speed bias can result in systematic error in emission estimates. In order to represent the impact of wind speed bias in the pseudo modeling data in the OSSEs, we apply a factor (k) to the simulated ffX_{CO2} (pseudo truth), where:

$$k = \frac{\bar{u}}{\bar{u}+\Delta}, \tag{2.4}$$

$\bar{u}$ is the average wind speed over the domain, and Δ is the corresponding bias (in ms^{-1}). This factor assumes a single ratio over the entire domain but allows to increase/decrease the $ffXCO_2$ to represent the impact of negative/positive wind speed bias.

2.6 Emission optimization method

A Bayesian inversion method similar to that used by Pillai et al. (2015) is implemented, which optimizes parameters of $ffCO_2$ emissions with observational constraints to obtain the best consistency between modelled and observed ffX_{CO2} enhancements. Specifically, we optimize the emissions by adjusting a scaling factor (λ) upon the a priori emissions from the entire city, without modifying the spatial distribution. The integrated ffX_{CO2} signals along a latitudinal range of interest of OCO-2 tracks is used as the observational constraint, which can be represented as:

$$y_o = \int_{lat1}^{lat2} ffX_{CO2,o}\,,\ y_m = \int_{lat1}^{lat2} ffX_{CO2,m} \tag{2.5}$$

where y_o and y_m are the observed and modelled results, respectively. Here, $ffX_{CO2,o}$ is derived by subtracting the background X_{CO2} from observations, and $ffX_{CO2,m}$ is derived by interpolating the modeling results of the tracer tagged with fossil fuel emissions at the coincident geolocations of the observations. Compared to deriving the scaling factor with the least square error method using all the soundings, the integral ffX_{CO2} shows less sensitivity to wind direction error (Fig. S2 and Text S1.2).

For *n* pairs of observations and modeling results obtained with *n* OCO-2 tracks, the integrated enhancements can be represented as

$$\boldsymbol{y}_o = \boldsymbol{y}_m \cdot \lambda + \boldsymbol{\varepsilon}_o \tag{2.6}$$

Here the state vector has been simplified as a scaler, i.e. the scaling factor λ, and the Jacobian matrix that represents the sensitivity of the observations to the state vector is given by a vector $\boldsymbol{y}_m$. The term $\boldsymbol{\varepsilon}_o$ is an observational error vector, including errors in the OCO-2 measurements, forward model, and model parameters. It is assumed to follow the Gaussian distribution described with the error covariance matrix S_o. As the observation errors are assumed to be uncorrelated for different tracks, S_o is a diagonal matrix with the main diagonal entries representing the error variance of the observation (σ^2_o) for each track. As the measurement and model uncertainty are unbiased and not correlated, we estimate σ^2_o by adding the error variances:

$$\sigma^2_o = \sigma^2_{measurement} + \sigma^2_{model}. \quad (2.7)$$

where $\sigma^2_{measurement}$ is the measurement error variance, and σ^2_{model} is the forward model error variance. The estimations of these two terms are detailed in sections 2.1 and 2.5, respectively.

The posterior estimate of λ is derived by minimizing the cost function (J):

$$J(\lambda) = (\boldsymbol{y}_o - \boldsymbol{y}_m\lambda)^T S_o^{-1} (\boldsymbol{y}_o - \boldsymbol{y}_m\lambda) + (\lambda - \lambda_a)^2\sigma_a^{-2} \quad (2.8)$$

where σ_a^2 is the error variance of the prior estimate, λ_a. The prior estimate λ_a is set to unity. The prior emission uncertainty is set up based on reported estimations in literature, as the ODIAC 2015a data product did not provide uncertainty estimates. At annual scales, Gurney et al. (2019) investigated the difference between the ODIAC data and a high-resolution bottom-up estimate product (Hestia) in four U.S. urban areas, showing the differences of whole-city emissions ranging from -1.5% to +20.8%. Oda et al. (2019) found differences of about 40% by comparing a satellite-derived annual emissions product to a gridded national inventory at 25-km resolution. However, the uncertainty would become larger at a smaller time scale. Considering the variability in anthropogenic activities, e.g. different power demand on weekdays and weekends, weather-related events, domestic heating, and air conditioning, the day-to-day variability of 20 to 50% can be found in emission inventories. As most of the temporal patterns in current emission products are prescribed, and based on recent publications at different timescales, we suggest uncertainties of 50% at the daily timescale is a lower bound. As this work focuses on quantifying the whole-city emissions, we conservatively set the prior flux uncertainty σ_a to 20% for LA, since the emissions from the U.S. megacities are relatively well characterized. For Riyadh and Cairo,

the prior uncertainty is set to 40%, as the fuel consumptions are expected to have higher uncertainties than over the U.S.

By solving the minimum of *J*, the optimal estimate of scaling factor, $\hat{\lambda}$, and the posterior error variance, $\hat{\sigma}^2$ can be obtained as:

$$\hat{\lambda} = (\boldsymbol{y}_m{}^T S_o^{-1} \boldsymbol{y}_m + \sigma_a^{-2})^{-1} (\boldsymbol{y}_m{}^T S_o^{-1} \boldsymbol{y}_o + \sigma_a^{-2} \lambda_a) \quad (2.9)$$

$$\hat{\sigma}^2 = (\boldsymbol{y}_m{}^T S_o^{-1} \boldsymbol{y}_m + \sigma_a^{-2})^{-1}. \quad (2.10)$$

2.7 OSSEs: emission optimization using multiple tracks under different meteorological conditions

Given the limited amount of real OCO-2 overpasses and the observation geometry, OSSEs are implemented to examine the potential of using multiple OCO-2 tracks to constrain urban $ffCO_2$ emissions in a statistical prospective, which allows examining the performances under different atmospheric transport conditions. Specifically, we examine the relation between the number of available tracks and the emission estimate uncertainty.

For each city, we use a specified and typical OCO-2 ground track in nadir observation mode to extract the pseudo observations and pseudo modelling data, based on the hourly modeled ffX_{CO2}. We avoided random selection of tracks across the domain, as OCO-2 tracks repeat over time without major variations. As the OCO-2 overpasses are available only during daytime, we selected the modeling results during 09:00-15:00 LST with domain averaged surface wind speed ≥ 2 ms^{-1}. Additionally, for Riyadh and Cairo, in order to ensure that plume transections exist, the simulation results are also filtered with the angle from a plume axis to the typical track $\geq 10°$ and $\leq 170°$.

The prior emissions, i.e. the ODIAC data, are set as the true emissions in the OSSEs. Hence, pseudo observations of ffX_{CO2} are obtained by sampling from the modeled ffX_{CO2} at the locations of the 1-s averaged soundings along the typical track. The pseudo observations are assumed to be unbiased relative to the truth. A random error per sample has been added, following a Gaussian distribution with the standard deviation of 0.2 ppm representing the lower bound of the measurement errors (section 2.1).

The pseudo modeling data of ffX_{CO2} along the typical tracks are obtained in different ways for different cities. For Riyadh and Cairo, the pseudo modeling data are set directly to the modeled ffX_{CO2} sampled along the typical track. Thus, the posterior emission estimate would be unbiased, and the truth of scaling factor would be unity. For LA, as the positive wind speed bias has been seen with the comparison to surface observations, we apply a factor to the simulated ffX_{CO2} to represent the impact of wind speed bias on the pseudo modeling ffX_{CO2} (see equation 2.4), which lead to a biased posterior scaling factor as will be shown in the results. The transport model uncertainty is estimated with the same methods detailed in section 2.5. We note that the uncertainty in background X_{CO2} is not included in the observation errors.

The impact of numbers of available tracks (N = 1, …, 20) on emission estimate uncertainty is evaluated by a Monte-Carlo approach. For each number of tracks (N), we randomly select N pairs of tracks of pseudo observation and modeling data. The scaling factor is derived with the same inversion method (section 2.6) as used for the real tracks analyses. Probability distributions of scaling factor and the associated posterior uncertainty are obtained by repeating the random selection procedure.

3 Results

3.1 Local fossil fuel X_{CO2} enhancement (ffX_{CO2})

The ffX_{CO2} enhancement, defined as the enhancement in X_{CO2} associated with local fossil fuel emissions relative to the background concentration, is used to constrain emissions in this study. In this section, the ffX_{CO2} enhancements are shown for Riyadh, Cairo, and LA, estimated by the simulations of $ffCO_2$ tracers tagged with the ODIAC emissions. The results are compared to the observed enhancements derived from the OCO-2 X_{CO2} data, in order to evaluate the magnitude of ffX_{CO2}, i.e. to assess whether the signals of local emissions are robust and detectable. Note that the whole-city emissions from these three cities in the months of the selected tracks are about 3.1 Mt C mo^{-1}, 2.5~2.7 Mt C mo^{-1}, and 4.5~4.7 Mt C mo^{-1} based on the ODIAC data (see Table 3). The OCO-2 tracks shown in this section are chosen by examining the observed X_{CO2} and the simulated plumes, to ensure that the satellite overpasses are downwind of the city with X_{CO2} signals attributable to local emissions.

3.1.1 Comparison of modeled and observed ffX_{CO2}

Figure 4 shows the ffX_{CO2} enhancements derived over Riyadh on 27 and 29 December 2014. Overall, the modeled enhancements over this domain are pronounced and can be up to about 6 ppm (Figs. 4c and 4d), indicating signals that can be unambiguously detected from space, given the precision and accuracy of the OCO-2 observations. The modeled ffX_{CO2} distributions are characterized by elongated and non-Gaussian plume structures, mostly due to complex horizontal wind fields (Figs. 4c and 4d). By examining the simulated ffX_{CO2} at one hour earlier and one hour later, rapidly changing fine-scale structures can be seen (Fig. S4), indicating notable variations in the distributions of ffX_{CO2} over a few hours. It is also noteworthy that, to examine the impact of domain resolution on the simulated ffX_{CO2}, we compared the results of 1-km, 3-km, and 9-km spatial resolutions. Lower and smoother peaks can be seen for the coarser resolutions (see Fig. S5), which is expected given the larger aggregation errors of the emissions at the lower spatial resolution, particularly for intense point sources. This result suggests the necessity of using a high spatial resolution to reproduce the complex plume structures for the "plume cities".

Figures 4a and 4b show the modeled and observed X_{CO2} along the two tracks. Note that the simulated X_{CO2} shown in these plots is derived as the sum of background line derived with the OCO-2 data and the simulated ffX_{CO2}. The observed ffX_{CO2} enhancements reach ~1.5 ppm and ~2.0 ppm for these two tracks. The magnitudes of modeled ffX_{CO2} are generally in agreement with the observations, although there is a prominent spatial displacement of ~0.3° in latitude (~33.4 km, Fig. 4a) between the observed and simulated peaks on 27 December, and the modeled peak on 29 December is narrower than observed. The large spatial offset might be due to the satellite track transecting the edge of the plume in a nearly parallel way, so that the modeled ffX_{CO2} values are very sensitive to errors in horizontal wind field.

For Cairo, the local ffX_{CO2} enhancements are examined for five tracks on 28 February, 18 March, 19 May, 15 July, and 16 August 2015, respectively. As shown Fig. 5, the modeled ffX_{CO2} enhancements over Cairo are mostly < 3.0 ppm over the simulation domain, with some hotspots located

close to some intense sources (Fig. S3). In comparison to Riyadh, the ffX_{CO2} enhancements are overall smaller, as expected given the lower total $ffCO_2$ emission. Compared to the simulated ffX_{CO2}, the observed local enhancement peaks are mostly higher and narrower, especially for the tracks on 19 May and 15 July 2015, while the modeled enhancements are smoother and diffuser. Spatial displacements in the signals are also seen for the tracks on 28 February and 16 August 2015.

It is notable that the background X_{CO2} values represented with the background lines exhibit higher latitudinal gradients for most of the selected tracks over Cairo (Figs. 5a and 5b) compared to over Riyadh. The background line method used here provides likely reasonable estimations of the background X_{CO2}, as general agreements are seen between the observed and modeled results of the integrated ffX_{CO2} enhancements along the satellite track within the domain of interest, which can be seen in the inverse estimates of total emission scaling factors (see section 3.2). Hence, this result indicates the advantage of the background line method in deriving background X_{CO2} for satellite observations analyzed at a spatial scale relevant to constraining local emission sources. Neglecting the latitudinal gradients in background X_{CO2} could lead to biases in ffX_{CO2}, as well as in emissions derived from observations.

In respect of LA, the ffX_{CO2} enhancements on 6 July, 15 July, 7 August, 16 August, 10 October, and 12 October 2015 are examined with the OCO-2 data and modeled ffX_{CO2}. As shown in Fig. 6, the ffX_{CO2} over the domain can be up to ~3.0 ppm and varies notably depending on meteorological conditions, as well as variations in the emissions. In comparison to the ffX_{CO2} distributions over Riyadh and Cairo characterized by elongated plumes and rapid changing structures, the ffX_{CO2} distributions over LA are more spread and composed of multiple plumes, mostly trapped in the basin during daytime owing to the onshore winds and local terrain. The study by Hedelius et al. (2017) demonstrated persistent differences of ~0.8 ppm in X_{CO2} between two locations only 9 km apart within the LA basin induced by the steep terrain near the basin. Hence, topography plays a critical role in the distributions of ffX_{O2}.

Figure 7 shows the comparison of the modeled and observed X_{CO2} over LA. Note that the OCO-2 X_{CO2} retrievals north to the northern edge of the desert are excluded in the analysis, in order to avoid using the soundings with high warn levels owing to complex topography and high albedo of the desert area, as can be seen in Fig. S6. The thresholds for latitude are 35.21° N, 35.05° N, 35.20° N, 34.90° N, 35.25° N, and 35.01° N, respectively, determined by examining the observations along with terrain height. Again, the background line has been added to the modeled ffX_{CO2} to present the total values, i.e. the ffX_{CO2} can be seen by the increments above the background lines. Overall, the modeled ffX_{CO2} are smaller than observed, which is likely owing to the positive biases in the modeled wind speeds, and the possible underestimation of the emissions. Similar to Cairo, prominent latitudinal gradients in the background are seen for some tracks, e.g. on 15 July and 12 October 2015.

3.1.2 Transport model uncertainty of modeled ffX_{CO2}

The uncertainty in ffX_{CO2} related to the transport model error is an important source of uncertainty in inverse emission estimate. Here we evaluate the impact of transport model error for the above-mentioned OCO-2 tracks. Note that different error estimation methods are used for the "plume cities" and the "basin city".

For Riyadh and Cairo, the transport model uncertainty in ffX_{CO2} has been shown with the light red shadings in Figs. 4a, b and Figs. 5a, b, estimated with the plume transformation method, as detailed in section 2.5.1. Specifically, for each track the simulated plume is perturbed 10^4 times with random errors in wind speeds and wind directions. Due to the non-Gaussian nature of the simulated plumes, as well as the non-linearity of the sampling process, the perturbed plumes are also non-Gaussian. Hence, we used the interquartile range (difference between the 25^{th} and the 75^{th} percentiles) as the uncertainty spread. Note that the uncertainty spread near the domain border is not shown because of the large portion of missing data after transforming the plume, which can also be seen in Fig. 2. The uncertainty in the modeled ffX_{CO2} over Cairo is up to 0.5 ppm, and up to 1.2 ppm over Riyadh. Given that the same probability distribution estimations of wind speed and wind direction errors are used for both cities, the smaller transport model uncertainty in ffX_{CO2} over Cairo can be mostly attributed to its lower total

emission leading to both the smaller ffX_{CO2} signals and the lower uncertainty spread. Another reason could be the relative locations of the tracks against those plumes they transect.

To evaluate the transport model errors in the modeled ffX_{CO2} over LA, an ensemble of simulations has been carried out as described in section 2.5.2. The result has been shown by the light red shadings in Fig. 7. Note that this uncertainty spread is related to the random transport model error, therefore it is independent of the systematic negative bias of the modeled ffX_{CO2} mentioned above. As represented by the range between the minimum and maximum ffX_{CO2} among the ensemble members, the uncertainty spread is larger where the ffX_{CO2} is stronger, with the maximum uncertainty for each track ranging from 0.32 to 0.93 ppm. The uncertainty spread is found to be overall smaller compared to over Riyadh and comparable to over Cairo. Given that the whole-city emission is the largest for LA among these three cities, this result is likely related to the effect of local terrain trapping the $ffCO_2$ within the LA basin and making the uncertainty decrease, as well as differences in the uncertainty spreads of wind fields.

3.1.3 Integral ffX_{CO2} enhancement

In this work, we optimize the whole-city emissions using the latitudinal integral ffX_{CO2} enhancements. Hence, in this section we present the modeled integral ffX_{CO2} for each OCO-2 tracks shown in the above section, and reveal how the integral ffX_{CO2} relates to transport model errors.

Figure 8 shows the probability distributions of the simulated integral ffX_{CO2} for the tracks over Riyadh and Cairo. The distribution for each track are derived by sampling the plumes perturbed with random transport errors 10^4 times. The distributions are mostly non-Gaussian, due to the non-linearities in sampling transformed plumes at a specified track. To isolate the impact of transport model errors, we also show the normalized uncertainty spread, represented by the ratio between the interquartile range and the median. For Riyadh, the result shows bimodal distributions with normalized spread of 1.47 and 0.73 (Fig. 8a). In comparison, the results for Cairo show narrower, less skewed, and unimodal distributions of the modeled integral ffX_{CO2} (Fig. 8b). The narrowest distribution is seen for the track on 18 Mar 2015 with the smallest integral ffX_{CO2} among the five tracks. The normalized uncertainty

spreads range from 0.17 to 0.38, smaller compared to Riyadh. This result is consistent with what has been shown along the tracks (Figs. 4 and 5).

The large uncertainty spread over Riyadh can be attributed to the relative location of the track against the plume and structure of the plume. For example, on 27 December 2014, the large uncertainty spread is likely due to high sensitivity of the simulated ffX_{CO2} to transport errors, since the transection is at the edge of the plume. For the track on 29 December, strong ffX_{CO2} enhancements (>5.0 ppm) are found downwind of the track due to local accumulation. Those enhancements can be sampled if the wind speed is lower, corresponding to the peak centered at ~24 ppm in Fig. 8a. Hence, the uncertainty spread also turned out to be large. Thus, it can be concluded that, the transport model uncertainty in the integral ffX_{CO2} is related to combined impacts of the magnitude of prior emissions, errors in winds, transection location relative to a plume, and the plume structure.

For LA, the modeled integral ffX_{CO2} for each selected track are shown in Fig. 9, based on the 18 ensemble members. The normalized uncertainty spread ranges between 0.06 ~ 0.28, smaller than the results over Riyadh and Cairo. This confirms the results shown earlier for the transport model uncertainty in ffXCO2 along tracks in section 3.1.2, suggesting again that the trapped dispersion by local terrain can make the transport model uncertainty in ffX_{CO2} smaller.

3.2 Emission estimates and uncertainty

In this section, we show the results of inverse emission estimates obtained by using the OCO-2 tracks shown in the above section for Riyadh, Cairo, and LA. Different sources of uncertainties are taken into consideration, including measurement errors and transport model errors. The inversions are preformed to derive scaling factors of total emissions over each of the selected cities. Note that the fluxes that can be retrieved or viewed from the X_{CO2} measurements vary from track to track, due to temporal variations in wind fields and emissions (Pillai et al., 2015). For example, if we consider an OCO-2 X_{CO2} sounding collected at 50 km downwind of the center of an urban emission area, it takes about 5 hours for air parcels to arrive travelling with a velocity of 3 m s^{-1}. In other words, the ffX_{CO2} obtained over or near an urban emission area can be determined by the emissions during several hours

ahead of the time of the overpass (Pillai et al., 2015). Given the overpass time of the OCO-2 in early afternoon (with the equatorial crossing time at 13:30 local time), the emission estimates constrained by the OCO-2 X_{CO2} measurements of each track could represent the emissions during morning to early afternoon on the date of the overpass. These should be taken into consideration when analyzing the results. The potential biases caused by the OCO-2 satellite observation strategy has been discussed in section 4.

The inversions are firstly implemented separately for every track among the selected ones. The inverse estimates of the emission scaling factor have been shown in Table 3, as well as the measurement and transport model uncertainties of the integral ffX_{CO2}, which are estimated with the methods described earlier in sections 2.1 and 2.5, respectively. Note that the prior scaling factor uncertainty, σ_a for LA has been set to a smaller value than those over Riyadh and Cairo, as in general there is a better knowledge of the emissions over the megacities in the U.S. (see also section 2.6).

The posterior scaling factors range between 0.92~0.83, 0.70~1.18, and 0.66~1.84 for the selected tracks over Riyadh, Cairo, and LA, respectively (Table 3), indicating notable temporal variations in the emission estimates from case to case. As has been explained, here the estimations represent emissions during a time period of several hours ahead of the time of overpass depending on the meteorological conditions. The posterior uncertainties, $\hat{\sigma}$ of the scaling factors for the three cities are found to range between 0.17~0.24, 0.10~0.25, and 0.11~0.16. The posterior scaling factor uncertainty has been shown overall larger for Riyadh and Cairo, compared to over LA.

With specified prior emission uncertainty for each city, the posterior uncertainty is related to both the measurement and transport model errors. The relative contribution of transport model uncertainty, σ_{model}, and measurement uncertainty, $\sigma_{measurement}$, are found to be different over the three cities. The σ_{model} values are for Riyadh are larger than the $\sigma_{measurement}$ by a factor of about 2 for the two tracks shown here (Table 3). By contrast, the σ_{model} for Cairo is generally smaller than the $\sigma_{measurement}$, consistent with what has been demonstrated in section 3.1.1. For LA, the relative magnitude of σ_{model} and $\sigma_{measurement}$ varies. The results show a larger σ_{model} than $\sigma_{measurement}$ for four among the six tracks

analyzed here. The spread of transport model uncertainty in ffX_{CO2} over LA is relatively smaller compared to over Riyadh, owing to likely the trapped dispersion within the basin, which is consistent with what has been shown earlier. It can be seen that, the transport model uncertainty is closely associated with the magnitude of urban emissions, relative location of plume and satellite track transection, transport model performance, and local topography. Variations of these factors lead to the temporal variability of the posterior emission uncertainty from track to track.

Although the inversion results of whole-city emissions have been demonstrated for each track separately, the sparseness of nearby OCO-2 tracks for many cities is still one of the main limitations to quantify emissions on a regular basis, as well as to track the temporal variations in emissions objectively from space. The numbers of useful tracks that have been analyzed in the above sections are two, five, and six over Riyadh, Cairo, and LA, respectively, which are chosen by examining the OCO-2 data during September 2014 to November 2015. Hence, we investigated the effect of using X_{CO2} data from two or more tracks on the inverse emission estimates. Given that there is no correlation between the observation uncertainties for any two tracks on different days, the ffX_{CO2} enhancement obtained from one track can not affect the emission on another day. Therefore, in order to investigate the effect of incorporating observations on different days, we derive one single scaling factor for all the days of the useful overpasses, as shown in Table 3. Note that the resulting scaling factor for each city would represent the best estimate of emission during several hours before the general time of local overpasses.

The resulting scaling factors (± 1σ uncertainty) are 0.85±0.16, 0.83±0.074 for Riyadh and Cairo (see Table 3), suggesting overestimation of emissions over those time periods the observations can represent by the prior emissions, i.e. the monthly ODIAC product. While for LA, the scaling factor (± 1σ uncertainty) is 1.36±0.074, indicating underestimation of the prior emission. As expected, the posterior uncertainty of scaling factor decreases substantially by using all the selected tracks over each city compared to the results with each track separately. The posterior uncertainties of the constrained whole-city emissions are reduced to about 19%, 9%, and 5% for the three cities, with the OCO-2 tracks obtained over about 1, 7, and 4 months, respectively. This result indicates the potential to obtain the

emission estimate with a lower uncertainty by utilizing OCO-2 tracks over a longer time period. As explained earlier, the inversion result is closely dependent on meteorological conditions and relative location of urban plume and satellite transection. Hence, we further investigate the performance of utilizing multiple OCO-2 tracks by the OSSEs (section 3.3).

3.3 Potential of constraining the emissions with multiple tracks

In this section, we explore the effect of multiple tracks of X_{CO2} measurements on constraining the $ffCO_2$ emissions. OSSEs are carried out for Riyadh, Cairo, and LA to examine the performance of OCO-2 like observations from a number of tracks (*N*) ranging from 2 to 20. In order to take scenes with meteorological conditions into consideration, we extract the pseudo observation and pseudo modeling data using all the hourly ffX_{CO2} modeling results in daytime for each city, rather than using only the modeling results close to the actual overpassing time. In this way we derived 217, 140, and 420 hours of ffX_{CO2} data in total, from which the tracks of pseudo data are generated accordingly (see section 2.7 for details). Note that the random error term used to generate pseudo observation ffX_{CO2} represent a lower bound of measurement uncertainty, and only the times with domain averaged surface wind speed ≥ 2 ms^{-1} are included. For Riyadh and Cairo, the pseudo data are further filtered with a criterion of the relative location of satellite transection upon ffX_{CO2} plume (see also section 2.7).

For a specific number of tracks (*N*), we randomly chose *N* tracks from the filtered pseudo data, and derive the scaling factor with these *N* tracks. It is assumed that, these *N* satellite tracks were collected over a time period during which there was no bias in the prior emissions. We use a Monte Carlo method to evaluate the general performance of multiple tracks by repeating the selection and inversion process for 10^3 times. Two tests T01 and T02 are defined here. For T01, only measurement error is applied to the pseudo data, and for T02 both measurement errors and transport model errors are included.

The posterior scaling factors retrieved with different numbers of tracks (*N*) are shown in Figs. 10a, 11a, and 12a for the three cities respectively. For Riyadh and Cairo, the median and average values are very close to the truth, i.e. one, for both T01 and T02, which can be expected given that the transport

model and measurement errors are assumed to be unbiased. While for LA, the median and average values are around 1.1, suggesting an overestimation by about 10% relative to the truth. This can be attributed to the overall underestimation in ffX_{CO2} due to the positive bias in the modeled wind speed. Variability of the retrieved scaling factors for different scenes and a specified *N* can be seen from the height of each box, i.e. the interquartile range, and the range between whiskers extending to the most extreme value that is not an outlier. Consistently for the three cities, the spread is found to be not obviously affected by the model errors, but mainly related to the random measurement errors. The spread becomes less and less with *N* increasing from 2 to 20, indicating that the measurement errors tend to have less impact of biasing the emission estimate when we have more data to constrain the emission.

Additionally, the posterior uncertainty of scaling factor is found to become smaller when the number of tracks increases (see Figs. 10b, 11b, and 12b). As expected, the posterior uncertainty is overall larger for T02 in comparison to T01, suggesting the prominent contribution of the transport model errors. For each box, 75% of data are lower than the top edge, i.e. the 3/4 quartile. The top whisker corresponds to about 3.275σ if the data are normally distributed, with more than 99.85% coverage below it. Hence for Riyadh, to retrieve the scaling factor with uncertainty <=0.1 (i.e. 10% uncertainty of total emission) with both the measurement and transport model errors considered, 5 or 8 tracks are needed at a confidence level of 75% or more than 99.85% (Fig. 10b). For Cairo the numbers are found to be lower, i.e. 3 or 5 at the two confidence levels (Fig. 11b), owing to the smaller transport errors that have been also shown for the inversions based on real tracks. For LA, we consider a lower threshold of posterior uncertainty of 5%, given that the knowledges prior emissions from the U.S. megacities are generally better, and the prior scaling factor uncertainty has already been set to 0.2. As shown in Fig. 12b, 5 or 7 tracks are needed to obtain the goal of 5% uncertainty at the two above-mentioned confidence levels. Note that in the OSSEs we have assumed no spatial correlation in the observation uncertainty. The number of tracks required to reduce the uncertainty would increase accordingly with the spatial correlation considered.

3.4 Impact of local biospheric CO_2 variations on the interpretation of local X_{CO2} enhancements

Forward simulations are carried out to investigate the influence of biospheric carbon fluxes on the interpretation of local X_{CO2} variation and the associated uncertainties. Two cases over the PRD region are analyzed using the simulation results and OCO-2 X_{CO2} obtained on January 15 and August 4, 2015, with the results shown in Fig. 13. These two cases correspond to conditions of fast atmospheric transport (i.e. high wind speeds) and weak transport (i.e. stagnant winds). The coastal circulation contrasts with the continental wind regimes, with fast winds over the sea on January 15 and near-zero wind speed on August 4, opposite to the inland circulation patterns. Because the $ffCO_2$ emissions come from several cities located in the PRD region, the modeled ffX_{CO2} are characterized by features of multiple overlapping plumes extending downwind from the major sources across the region.

To demonstrate the impact of local biospheric CO_2 variations on local X_{CO2} enhancements, we derive the local X_{CO2} enhancement (referred to as ΔX_{CO2}) from the simulated total X_{CO2} by subtracting the minimum value of the simulated results along a track. The constant background is valid for the simulation results, as the spatial gradient in the background concentration is negligible due to a constant boundary condition is used in the simulations. The observed ΔX_{CO2} is extracted using the same method as the preceding sections. As can be seen in Fig. 13, overall the simulated local enhancements including biospheric X_{CO2} signals are larger than the simulated ffX_{CO2}, and show a better agreement with the observed ΔX_{CO2}. Imposed by NEE from 15 MsTMIP biospheric models, the spread of simulated ΔX_{CO2} indicates the uncertainty in the local enhancement associated with the uncertainty in biospheric fluxes. Considering the tracks shown in Fig. 13, , the biogenic X_{CO2} variability at local scales account for ~32±27% (1σ) and ~24±18% (1σ) of the latitudinally integrated local enhancement, respectively. In other words, if the biospheric signal is not separated from the local ffX_{CO2} enhancements, the total emissions would be overestimated by about 47±37% and 32±22% for the two cases examined here.

For Riyadh and Cairo, the biospheric contribution is negligible compared to the local fossil fuel signals, since the local spatial gradient of NEE is much smaller than the $ffCO_2$ emission. Therefore, simulations for the two cities are not shown. But we note that biogenic fluxes for Cairo (Nile River

delta) might be underestimated by the vegetation models. For LA, there are two reasons for not implementing a simulation like the PRD. First, the default MODIS-based GVF climatological maps in WRF shows nonrealistic values compared with the real-time MODIS-based GVF maps derived by Vahmani and Ban-Weiss (2016) (Fig. S7). Second, NEE is downscaled assuming a constant vegetation productivity within a single NEE grid cell (0.5°×0.5°). However, LA has a variety of climate zones because of its proximity to the Pacific Ocean and the nearby mountain ranges, where a variety of vegetation species exist with different growth patterns (McPherson et al., 2008). Thus, it could be unreasonable to assume a constant productivity. Also, a study based on in-situ flask observations in LA of $^{14}CO_2$ indicated about 25% biogenic contributions to the mid-day CO_2 enhancement (Miller et al., 2017), in agreement with Newman et al. (2016), but poorly simulated by vegetation model (Feng et al., 2016). More comprehensive data and method are needed to fulfill the estimation of biospheric contribution.

4 Discussion

4.1 Challenges for other cities

In this paper, typical cities with different local topography features are examined, which are selected following the criteria in section 2.3. The simulations over Riyadh and LA demonstrate ffX_{CO2} enhancements overall larger than 1.0 ppm and up to about 6.0 ppm, greater than the uncertainty of retrievals over land (~1 ppm) (Eldering et al., 2017a). However, for Cairo the ffX_{CO2} values are mostly < 3.0 ppm with some hotspots near the large emission sources. For some smaller cities, it would be even challenging to optimize their emissions from space due to limited detectability of fossil-fuel imprints. The factors limiting the detectability would include: i) large cloud coverage obscuring the sensor; ii) occasional high anthropogenic aerosol loading leading to larger measurement uncertainty; iii) overlapping enhancements from other cities or point sources nearby; and iv) low $ffCO_2$ emission. To obtain a bigger chance of unambiguously detecting plumes from cities, an imaging satellite with a

wider swath and sufficient precision like the concept of CarbonSat (Buchwitz et al., 2013; ESA, 2015) would be helpful.

Another challenge for many cities is to interpret and distinguish local X_{CO2} variations introduced by the biospheric fluxes and fossil fuel emissions. In this work, the variations resulting from the inhomogeneity of local biospheric fluxes have been evaluated by the simulations in section 3.4. Similarly, Dayalu et al. (2017) showed equivalent magnitudes of the vegetation and the anthropogenic signal with the Vegetation, Photosynthesis, and Respiration Model (VPRM) simulations at a surface observation site in Northern China. We note that the NEE data used in this work still need further verification for regions and seasons. In addition, the downscaling of NEE data is based on the assumption of uniform local vegetation productivity, while some studies have reported impact of human interventions on urban vegetation (Hutyra et al., 2014). For example, fertilization is likely to increase both Gross Primary Productivity (GPP) and respiration of ecosystems in urban areas compared to their natural counterparts. Given the limitation in biosphere models, many observational data have been used to extract $ffCO_2$ signals against the large and varying background, e.g. measurements of co-emitted components such as CO and NO_x (Reuter et al., 2014; Silva et al., 2013; Turnbull et al., 2011b) with efforts to determine the emission ratios accurately. Additionally, the radiocarbon content of CO_2 ($^{14}CO_2$) (Turnbull et al., 2015, 2016) has been used, although existing technology limits $^{14}CO_2$ measurement to laboratory-based analysis of individual samples at low sampling resolution. These data could provide more constraints of $ffCO_2$ emissions when assimilated in the inversion system jointly.

4.2 Insights from results of the OSSEs

The performance of multiple tracks on retrieving the scaling factor of whole-city emission has been evaluated by the OSSEs, with transport model errors and measurement errors considered. The results suggest the potential of obtaining emission estimates at a lower uncertainty level and over a longer time window. At a confidence level of more than 99.85%, the estimated least number of tracks required to constrain the total emissions for Riyadh (<10% uncertainty), Cairo (<10%), and LA (<5%) are 5, 8, and 7, respectively. As the pseudo tracks represent different meteorological conditions, the OSSEs' results

can indicate the potential of OCO-2 data in the long run. For example, we examined the number of available tracks over the three cities by counting the tracks located downwind of city and captured peaks in X_{CO2} using OCO-2 data and surface horizontal wind data in NCEP FNL during September 2014 to November 2015, i.e. 15 months in total. There are 8 (13, 17) tracks over Riyadh (Cairo, LA) matching the criteria, corresponding to about one track per 1.75 (1.08, 0.82) months. Therefore, the general time it takes to collect the above-mentioned number of tracks would be about 14, 5, and 6 months over the three cities. It takes the longest time for Riyadh, which can be likely owing to the relatively larger emission than Cairo, and the less complex terrain than LA. With some other satellite missions being planned and carried out, a shorter time can be expected to retrieve emissions at the uncertainty of policy-relevant level.

Positive bias in the emission scaling factor is found for LA, while the estimates are centered at the truth for Riyadh and Cairo. We suspect that the emission bias resulted from mostly the propagation of the positive wind speed bias in the WRF atmospheric model over LA, as the wind speed bias has been considered when constructing the pseudo modeling data. In comparison, the WRF simulations over plume cities located in flat terrain show better results of wind speed and direction, e.g. wind speed errors of <1 m/s are reported for modeling results without data assimilation over Indianapolis (Deng et al., 2017), and <0.8 m/s around Paris (Lac et al., 2013). Data assimilation systems are proven to be useful to significantly improve model performances with decreased systematic errors (<0.5 m/s) (Deng et al., 2017), which can be an effective way of reducing the wind biases for basin cities (Ware et al., 2016).

4.3 Remaining error components in the inverse emission estimates

In addition to the uncertainties in transport model, OCO-2 measurements, and biospheric fluxes, there are several sources of errors remaining to be considered. First, the measurement errors of OCO-2 data are assumed to be non-correlated spatially, as the correlations are yet to be characterized at high resolution at present. Additionally, the nonlinearities in the retrievals and the random components of interference errors (Connor et al., 2016) and imperfection in cloud screening especially for low clouds

(Taylor et al., 2016) could also introduce large errors in the retrievals. We note that in the OSSEs, the measurement uncertainty has been evaluated using a lower bound of the uncertainty.

For the emission inversion system, the prior emissions have been assumed to be perfectly distributed and optimized with a whole-city scaling factor. As noted by Pillai (2015), the flexibility to capture the true spatial variation of fluxes is more limited in the inversion system with one scaling factor for entire city, compared to in pixel- or parameter-wise inversions. However, the pixel-level emission uncertainties would be significantly larger than those of the whole-city emissions. Assessment of prior emissions errors in gridded field is difficult (Andres et al., 2016), which is usually done by comparing emission inventories at an aggregated spatial resolution (Hutchins et al., 2017; Oda et al., 2015). The ODIAC data have been compared to the Hestia emission product (Gurney et al., 2019), which is one of the most accurate and complete emission inventories at the scale of buildings and street segments as evaluated against in situ tower measurements (Lauvaux et al., 2016). At 1 km × 1 km spatial scale, the result reveals a low-emission limit in ODIAC driven by saturation of the nighttime light spatial proxy, and the median difference ranging between 47 to 84%. The largest discrepancies were found for large point sources and the on-road sector. More studies on emission comparisons would allow us to realistically constrain the emissions at sector and pixel levels.

Additionally, we note that the temporal representation of emission estimates by OCO-2 measurements can be limited given the sampling strategy. As the satellite measurements are only available in daytime clear-sky scenes, X_{CO2} can not be evenly sampled in time. This makes it difficult to quantify the diurnal variability in the emissions. It is suggested that X_{CO2} retrievals must be taken into inversion modeling at the original temporal and spatial representativity (Corbin and Denning, 2006), since the clear-sky sampling biases the X_{CO2} if they are used as daily values or averaged over a longer time period. To estimate the effect of sampling bias, we calculated the daily emission from Indianapolis by using data during daytime hours (09:00-14:00 LST) and clear-sky daytime hours, based on the hourly emission of the Hestia product (Gurney et al., 2012) for a full year and cloud cover data from a surface synoptic observation site nearby. The average daily emission for daytime hours has a

+14% bias compared to the actual Hestia emissions estimate including all hours. In addition, the bias increases to +28% when sampling only days with clear-sky conditions. Therefore, the retrieved emissions using OCO-2 measurements would be overall larger than the daily average. As another estimation, we examined the diurnal variability pattern of emissions estimated by Nassar et al. (2013). For Riyadh, Cairo and LA, the ratios between emission at about the satellite overpassing time against the monthly average value are about 1.195, 1.127 and 1.288, corresponding to biases of about +19.5%, +12.7% and +28.8% by only sampling in daytime compared to the monthly total emissions. More space observation missions including the Geostationary Carbon Cycle Observatory (GeoCarb) (Moore et al., 2018), OCO-3 (Eldering et al., 2017b), and MicroCARB (https://microcarb.cnes.fr/en/MICROCARB/GP_mission.htm) will further enhance the uniform sampling over urban areas.

5 Conclusions

In this paper, we presented the potential of using X_{CO2} observations from OCO-2 to optimize the $ffCO_2$ emission from urban areas. High-resolution forward modeling of the atmospheric transport has been implemented to reproduce fine-scale structures of ffX_{CO2} plumes, as well as to link emissions with observed X_{CO2}. The contributions of transport model errors, measurement errors, and local variability of biospheric fluxes on the inverse estimates of whole-city emissions have been evaluated.

We used a Bayesian inversion approach to optimize the $ffCO_2$ emissions from three cities (Riyadh, Cairo, and Los Angeles), using the OCO-2 tracks with detectable enhancements collected between September 2014 to November 2015, namely 15 months in total. The retrieved scaling factors ranged between 0.92~0.83, 0.70~1.18, and 0.66~1.84 for the three cities, indicating notable temporal variations in the inverse emissions from day to day. The posterior uncertainties were largest for Riyadh, mostly due to the transport model uncertainty. Prominent variability of posterior scaling factor uncertainties for the individual tracks was also due to varying meteorological conditions and locations of satellite tracks relative to city plumes. By incorporating all the selected tracks for each city, the

posterior uncertainty of scaling factor was found to decrease substantially, corresponding to about 19%, 9%, and 5% uncertainty of the posterior emissions. This indicates a potential to improve current emissions estimates by utilizing OCO-2 tracks over a time period, since the frequency of nearby OCO-2 measurements is limited for each city.

We evaluated the potential of using multiple OCO-2 tracks by performing pseudo-data experiments based on the high-resolution forward simulation results for the real cases analyzed above, taking the impacts of both measurement errors and transport model errors into account. For a certain number of tracks, it's assumed here that those satellite tracks were collected over a time period, during which there was no bias in the prior emissions. As revealed by the experiments, to obtain posterior uncertainty <=0.1 (i.e. 10% uncertainty of total emission), 5 or 8 (3 or 5) tracks are needed for Riyadh (Cairo), at a confidence level of 75% or more than 99.85%. For LA, we consider a lower threshold of the posterior uncertainty of 5%, and 5 or 7 tracks are needed to achieve this goal at 75% or 99.85% confidence level.

The impact of local variability in biospheric fluxes on spatial X_{CO2} variations is evaluated, with the uncertainty of the biospheric fluxes represented by using downscaled fluxes from the 15 biosphere models adopted in the MsTMIP inter-comparison. Despite the large $ffCO_2$ emissions from the Pearl River Delta, significant fractions, i.e. 32±27% (1σ) and 24±18% (1σ) for the two cases shown, of the local X_{CO2} enhancements are driven by the local biogenic fluxes. This would lead to overestimation of total emissions by about 47±37% and 32±22%. For cities with biospheric fluxes of comparable magnitude but smaller fossil-fuel emissions, the contribution is expected to be larger than the values shown above. Therefore, for the cities in mid-latitudes and the equatorial areas with prominent local and regional biospheric fluxes, the biospheric contribution is essential for appropriate interpretation of the X_{CO2} retrievals.

For future improvements of the quantification and monitoring of urban $ffCO_2$ emissions with OCO-2 data or other polar-orbit measurements, temporal and spatial correlations in prior emissions errors will likely be critical terms to be considered, which are not included in the inversions here. Given the limited satellite overpasses owing to cloud cover, retrieval issues, sampling geometry, and satellite

revisiting cycle, etc, the information on prior emissions error correlations will allow us to retrieve the temporal variations and spatial structures of emissions in a more effective way, compared to using one scaling factor for the entire city. In that case, the appropriate number of tracks to constrain urban emissions will depend on the granularity, i.e. the spatio-temporal resolutions of emissions in a target city, as well as the precision level required to inform policy decisions.

In addition, compared to the long-term trends in emissions that are more easily detectable, biases in retrieved emissions due to daytime-only sampling are somewhat difficult to be recovered with observations similar to OCO-2 data. Fortunately, with the continuing OCO-2 observations during its extended mission and space-based CO_2 measurement missions being deployed and planned with geostationary observations or targeting strategy over cities, the CO_2 records will be extended to potentially allow us to achieve emissions with a better temporal representativity. Our results in this work indicate a promising potential of measurements from OCO-2 or similar missions to constrain urban emissions for cities with robust ffX_{CO2} enhancements, by using high-resolution transport modeling and the inversion approach. It can be expected that, the OCO-2 data would be more effectively used to improve the accuracy and precision of urban fossil fuel carbon fluxes, in combination with observations from other platforms to support emission reduction strategies.

Acknowledgments

This work has been funded jointly by the National Aeronautics and Space Administration (NASA), Orbiting Carbon Observatory 2 (OCO-2) project (award NNX15AI42G), the National Institute for Standards and Technology (NIST) Indianapolis Flux Experiment (INFLUX) project (award 70NANB10H245), the National Oceanic and Atmospheric Administration (NOAA) project (grant NA13OAR4310076), the French research program *Make Our Planet Great Again*, and the National Science Foundation Graduate Research Fellowship grant (DGE 1256260). The Level 2 OCO-2 XCO2 (version v7r) data used in this study are archived in permanent repository at NASA's Goddard Space

Flight Center's Earth Sciences Data and Information Services Center (GES-DISC), and are also available at NASA's Jet Propulsion Laboratory (http://co2.jpl.nasa.gov).

References

Ackerman, K. V., & Sundquist, E. T. (2008). Comparison of two U.S. power-plant carbon dioxide emissions data sets. *Environmental Science & Technology*, *42*(15), 5688–5693. https://doi.org/10.1021/es800221q

Andres, R. J., Boden, T. A., Bréon, F.-M., Ciais, P., Davis, S., Erickson, D., … Treanton, K. (2012). A synthesis of carbon dioxide emissions from fossil-fuel combustion. *Biogeosciences*, *9*(5), 1845–1871. https://doi.org/10.5194/bg-9-1845-2012

Andres, R. J., Boden, T. A., & Higdon, D. M. (2016). Gridded uncertainty in fossil fuel carbon dioxide emission maps, a CDIAC example. *Atmospheric Chemistry and Physics*, *16*(23), 14979–14995. https://doi.org/10.5194/acp-16-14979-2016

Angevine, W. M., Eddington, L., Durkee, K., Fairall, C., Bianco, L., & Brioude, J. (2012). Meteorological model evaluation for CalNex 2010. *Monthly Weather Review*, *140*(12), 3885–3906. https://doi.org/10.1175/MWR-D-12-00042.1

Barkley, Z. R., Lauvaux, T., Davis, K. J., Deng, A., Miles, N. L., Richardson, S. J., … Maasakkers, J. D. (2017). Quantifying methane emissions from natural gas production in north-eastern Pennsylvania. *Atmos. Chem. Phys*, *17*, 13941–13966. https://doi.org/10.5194/acp-17-13941-2017

Bougeault, P., & Lacarrere, P. (1989). Parameterization of orography-induced turbulence in a mesobeta-scale model. *Monthly Weather Review*, *117*(8), 1872–1890. https://doi.org/10.1175/1520-0493(1989)117<1872:POOITI>2.0.CO;2

Bousquet, P. (2000). Regional changes in carbon dioxide fluxes of land and oceans since 1980. *Science*, *290*(5495), 1342–1346. https://doi.org/10.1126/science.290.5495.1342

Bovensmann, H., Burrows, J. P., Buchwitz, M., Frerick, J., Noël, S., Rozanov, V. V., … Goede, A. P. H. (1999). SCIAMACHY: Mission objectives and measurement modes. *Journal of the Atmospheric Sciences*, *56*(2), 127–150. https://doi.org/10.1175/1520-0469(1999)056<0127:SMOAMM>2.0.CO;2

Boxe, C. S., Worden, J. R., Bowman, K. W., Kulawik, S. S., Neu, J. L., Ford, W. C., … Oltmans, S. J. (2010). Validation of northern latitude Tropospheric Emission Spectrometer stare ozone profiles with ARC-IONS sondes during ARCTAS: sensitivity, bias and error analysis. *Atmospheric Chemistry and Physics*, *10*(20), 9901–9914. https://doi.org/10.5194/acp-10-9901-2010

Bréon, F. M., Broquet, G., Puygrenier, V., Chevallier, F., Xueref-Remy, I., Ramonet, M., … Ciais, P. (2015). An attempt at estimating Paris area CO_2 emissions from atmospheric concentration measurements. *Atmospheric Chemistry and Physics*, *15*(4), 1707–1724. https://doi.org/10.5194/acp-15-1707-2015

Briber, B., Hutyra, L., Dunn, A., Raciti, S., & Munger, J. (2013). Variations in atmospheric CO_2 mixing ratios across a Boston, MA urban to rural gradient. *Land*, *2*(3), 304–327. https://doi.org/10.3390/land2030304

Buchwitz, M., de Beek, R., Noël, S., Burrows, J. P., Bovensmann, H., Bremer, H., … Heimann, M. (2005). Carbon monoxide, methane and carbon dioxide columns retrieved from SCIAMACHY by WFM-DOAS: year 2003 initial data set. *Atmospheric Chemistry and Physics*, *5*(12), 3313–3329. https://doi.org/10.5194/acp-5-3313-2005

Buchwitz, M., Reuter, M., Bovensmann, H., Pillai, D., Heymann, J., Schneising, O., … Löscher, A. (2013). Carbon Monitoring Satellite (CarbonSat): assessment of atmospheric CO_2 and CH_4 retrieval errors by error parameterization. *Atmospheric Measurement Techniques*, *6*(12), 3477–3500. https://doi.org/10.5194/amt-6-3477-2013

Cambaliza, M. O. L., Shepson, P. B., Caulton, D. R., Stirm, B., Samarov, D., Gurney, K. R., …

Richardson, S. J. (2014). Assessment of uncertainties of an aircraft-based mass balance approach for quantifying urban greenhouse gas emissions. *Atmospheric Chemistry and Physics*, *14*(17), 9029–9050. https://doi.org/10.5194/acp-14-9029-2014

Ciais, P., Rayner, P., Chevallier, F., Bousquet, P., Logan, M., Peylin, P., & Ramonet, M. (2010). Atmospheric inversions for estimating CO_2 fluxes: methods and perspectives. *Climatic Change*, *103*(1–2), 69–92. https://doi.org/10.1007/s10584-010-9909-3

Ciais, P., Sabine, C., Bala, G., Bopp, L., Brovkin, V., Canadell, J., … Thornton, P. (2013). Carbon and other biogeochemical cycles. In Intergovernmental Panel on Climate Change (Ed.), *Climate Change 2013 - The Physical Science Basis* (pp. 465–570). Cambridge: Cambridge University Press. https://doi.org/10.1017/CBO9781107415324.015

Connor, B., Bösch, H., Mcduffie, J., Taylor, T., Fu, D., Frankenberg, C., … Oyafuso, F. (2016). Quantification of uncertainties in OCO-2 measurements of XCO_2 : simulations and linear error analysis. *Atmospheric Measurement Techniques*, *9*, 5227–5238. https://doi.org/10.5194/amt-9-5227-2016

Corbin, K. D., & Denning, A. S. (2006). Using continuous data to estimate clear-sky errors in inversions of satellite CO_2 measurements. *Geophysical Research Letters*, *33*(12), L12810. https://doi.org/10.1029/2006GL025910

Corbin, K. D., Denning, A. S., & Gurney, K. R. (2010). The space and time impacts on U.S. regional atmospheric CO2 concentrations from a high resolution fossil fuel CO2 emissions inventory. *Tellus, Series B: Chemical and Physical Meteorology*, *62*(5), 506–511. https://doi.org/10.1111/j.1600-0889.2010.00480.x

Crisp, D. (2008). NASA Orbiting Carbon Observatory: measuring the column averaged carbon dioxide mole fraction from space. *Journal of Applied Remote Sensing*, *2*(1), 023508. https://doi.org/10.1117/1.2898457

Crisp, D. (2015). Measuring atmospheric carbon dioxide from space with the Orbiting Carbon Observatory-2 (OCO-2). In J. J. Butler, X. (Jack) Xiong, & X. Gu (Eds.), *SPIE 9607 Earth Observing Systems* (p. 960702). South Kensington Campus. https://doi.org/10.1117/12.2187291

Crisp, D., Atlas, R. M., Breon, F.-M., Brown, L. R., Burrows, J. P., Ciais, P., … Schroll, S. (2004). The Orbiting Carbon Observatory (OCO) mission. *Advances in Space Research*, *34*(4), 700–709. https://doi.org/10.1016/j.asr.2003.08.062

Davis, K. J., Deng, A., Lauvaux, T., Miles, N. L., Richardson, S. J., Sarmiento, D. P., … Karion, A. (2017). The Indianapolis Flux Experiment (INFLUX): A test-bed for developing urban greenhouse gas emission measurements. *Elem Sci Anth*, *5*, 21. https://doi.org/10.1525/elementa.188

Dayalu, A., Munger, W., Wofsy, S. C., Wang, Y., Nehrkorn, T., Zhao, Y., … Luus, K. (2017). VPRM-CHINA: Using the Vegetation, Photosynthesis, and Respiration Model to partition contributions to CO_2 measurements in Northern China during the 2005-2009 growing seasons. *Biogeosciences Discussions*, (12), 1–29. https://doi.org/10.5194/bg-2017-504

Deng, A., Lauvaux, T., Davis, K. J., Gaudet, B. J., Miles, N., Richardson, S. J., … Gurney, K. R. (2017). Toward reduced transport errors in a high resolution urban CO_2 inversion system. *Elem Sci Anth*, *5*, 20. https://doi.org/10.1525/elementa.133

Diaz-Issac, L., Lauvaux, T., Bocquet, M., & Davis, K. J. (2018). Calibration of a multi-physics ensemble for greenhouse gas atmospheric transport model uncertainty estimation. *Atmospheric Chemistry and Physics Discussions*, https://doi.org/10.5194/acp-2018-1117.

Duren, R. M., & Miller, C. E. (2012). Measuring the carbon emissions of megacities. *Nature Climate Change*, *2*(8), 560–562. https://doi.org/10.1038/nclimate1629

Eldering, A., O'Dell, C. W., Wennberg, P. O., Crisp, D., Gunson, M. R., Viatte, C., … Yoshimizu, J. (2017a). The Orbiting Carbon Observatory-2: first 18 months of science data products.

Atmospheric Measurement Techniques, *10*(2), 549–563. https://doi.org/10.5194/amt-10-549-2017

Eldering, A., Wennberg, P. O., Crisp, D., Schimel, D. S., Gunson, M. R., Chatterjee, A., … Weir, B. (2017b). The Orbiting Carbon Observatory-2 early science investigations of regional carbon dioxide fluxes. *Science*, *358*(6360), eaam5745. https://doi.org/10.1126/science.aam5745

Engelen, R. J., Serrar, S., & Chevallier, F. (2009). Four-dimensional data assimilation of atmospheric CO_2 using AIRS observations. *Journal of Geophysical Research*, *114*(D3), D03303. https://doi.org/10.1029/2008JD010739

ESA. (2015). *CarbonSat, ESA SP-1330/1 (2 volume series)*. Noordwijk, The Netherlands. Retrieved from http://esamultimedia.esa.int/docs/EarthObservation/SP1330-1_CarbonSat.pdf

Feng, S., Lauvaux, T., Newman, S., Rao, P., Ahmadov, R., Deng, A., … Yung, Y. L. (2016). Los Angeles megacity: a high-resolution land–atmosphere modelling system for urban CO_2 emissions. *Atmospheric Chemistry and Physics*, *16*(14), 9019–9045. https://doi.org/10.5194/acp-16-9019-2016

Fisher, J. B., Sikka, M., Huntzinger, D. N., Schwalm, C., & Liu, J. (2016). Technical note: 3-hourly temporal downscaling of monthly global terrestrial biosphere model net ecosystem exchange. *Biogeosciences*, *13*(14), 4271–4277. https://doi.org/10.5194/bg-13-4271-2016

Gately, C. K., & Hutyra, L. R. (2017). Large uncertainties in urban-scale carbon emissions. *Journal of Geophysical Research: Atmospheres*, *122*(20), 11,242-11,260. https://doi.org/10.1002/2017JD027359

Grell, G. A., Peckham, S. E., Schmitz, R., McKeen, S. A., Frost, G., Skamarock, W. C., & Eder, B. (2005). Fully coupled “online” chemistry within the WRF model. *Atmospheric Environment*, *39*(37), 6957–6975. https://doi.org/10.1016/j.atmosenv.2005.04.027

Gurney, K. R., Mendoza, D. L., Zhou, Y., Fischer, M. L., Miller, C. C., Geethakumar, S., & de la Rue du Can, S. (2009). High resolution fossil fuel combustion CO_2 emission fluxes for the United

States. *Environmental Science & Technology*, *43*(14), 5535–5541. https://doi.org/10.1021/es900806c

Gurney, K. R., Razlivanov, I., Song, Y., Zhou, Y., Benes, B., & Abdul-Massih, M. (2012). Quantification of fossil fuel CO_2 emissions on the building/street scale for a large U.S. city. *Environmental Science & Technology*, *46*(21), 12194–12202. https://doi.org/10.1021/es3011282

Gurney, K. R., Romero-Lankao, P., Seto, K. C., Hutyra, L. R., Duren, R., Kennedy, C., … Sperling, J. (2015). Climate change: Track urban emissions on a human scale. *Nature*, *525*(7568), 179–181. https://doi.org/10.1038/525179a

Gurney, K. R., Liang, J., O'Keeffe, D., Patarasuk, R., Hutchins, M., Huang, J., … Song, Y. (2019). Comparison of Global Downscaled Versus Bottom-Up Fossil Fuel CO_2 Emissions at the Urban Scale in Four U.S. Urban Areas. *Journal of Geophysical Research: Atmospheres*, *124*(5), 2823–2840. https://doi.org/10.1029/2018JD028859

Hakkarainen, J., Ialongo, I., & Tamminen, J. (2016). Direct space-based observations of anthropogenic CO_2 emission areas from OCO-2. *Geophysical Research Letters*, *43*(21), 11,400-11,406. https://doi.org/10.1002/2016GL070885

Hedelius, J. K., Feng, S., Roehl, C. M., Wunch, D., Hillyard, P. W., Podolske, J. R., … Wennberg, P. O. (2017). Emissions and topographic effects on column CO_2 (XCO_2) variations, with a focus on the Southern California Megacity. *Journal of Geophysical Research: Atmospheres*, *122*(13), 7200–7215. https://doi.org/10.1002/2017JD026455

Hogue, S., Marland, E., Andres, R. J., Marland, G., & Woodard, D. (2016). Uncertainty in gridded CO_2 emissions estimates. *Earth's Future*, *4*(5), 225–239. https://doi.org/10.1002/2015EF000343

Houweling, S., Aben, I., Breon, F.-M., Chevallier, F., Deutscher, N., Engelen, R., … Serrar, S. (2010). The importance of transport model uncertainties for the estimation of CO_2 sources and sinks using satellite measurements. *Atmospheric Chemistry and Physics*, *10*(20), 9981–9992.

https://doi.org/10.5194/acp-10-9981-2010

Huntzinger, D. N., Schwalm, C., Michalak, A. M., Schaefer, K., King, A. W., Wei, Y., … Zhu, Q. (2013). The North American carbon program multi-scale synthesis and terrestrial model Intercomparison Project – Part 1: Overview and experimental design. *Geoscientific Model Development*, *6*(6), 2121–2133. https://doi.org/10.5194/gmd-6-2121-2013

Hutchins, M. G., Colby, J. D., Marland, G., & Marland, E. (2017). A comparison of five high-resolution spatially-explicit, fossil-fuel, carbon dioxide emission inventories for the United States. *Mitigation and Adaptation Strategies for Global Change*, *22*(6), 947–972. https://doi.org/10.1007/s11027-016-9709-9

Hutyra, L. R., Duren, R., Gurney, K. R., Grimm, N., Kort, E. A., Larson, E., & Shrestha, G. (2014). Urbanization and the carbon cycle: Current capabilities and research outlook from the natural sciences perspective. *Earth's Future*, *2*(10), 473–495. https://doi.org/10.1002/2014EF000255

Idso, C. D., Idso, S. B., & Balling Jr., R. C. (1998). The urban CO_2 dome of Phoenix, Arizona. *Physical Geography*, *19*, 95–108. https://doi.org/10.1080/02723646.1998.10642642

International Energy Agency. (2008). *World Energy Outlook*. IEA. https://doi.org/10.1787/weo-2016-en

IPCC. (2006). *2006 IPCC Guidelines for National Greenhouse Gas Inventories*. *Institute for Global Environmental Strategies*. Hayama, Kanagawa, Japan. https://doi.org/10.1007/978-1-60327-310-7

Janardanan, R., Maksyutov, S., Oda, T., Saito, M., Kaiser, J. W., Ganshin, A., … Yokota, T. (2016). Comparing GOSAT observations of localized CO_2 enhancements by large emitters with inventory-based estimates. *Geophysical Research Letters*, *43*(7), 3486–3493. https://doi.org/10.1002/2016GL067843

Janjić, Z. I. (1994). The step-mountain eta coordinate model: further developments of the convection, viscous sublayer, and turbulence closure schemes. *Monthly Weather Review*, *122*(5), 927–945.

https://doi.org/10.1175/1520-0493(1994)122<0927:TSMECM>2.0.CO;2

Janssens-Maenhout, G., Dentener, F., Van Aardenne, J., Monni, S., Pagliari, V., Orlandini, L., … Keating, T. (2012). *EDGAR-HTAP: a harmonized gridded air pollution emission dataset based on national inventories*. https://doi.org/10.2788/14102

Keppel-Aleks, G., Wennberg, P. O., O'Dell, C. W., & Wunch, D. (2013). Towards constraints on fossil fuel emissions from total column carbon dioxide. *Atmospheric Chemistry and Physics*, *13*(8), 4349–4357. https://doi.org/10.5194/acp-13-4349-2013

Kort, E. A., Frankenberg, C., Miller, C. E., & Oda, T. (2012). Space-based observations of megacity carbon dioxide. *Geophysical Research Letters*, *39*(17). https://doi.org/10.1029/2012GL052738

Kurokawa, J., Ohara, T., Morikawa, T., Hanayama, S., Janssens-Maenhout, G., Fukui, T., … Akimoto, H. (2013). Emissions of air pollutants and greenhouse gases over Asian regions during 2000–2008: Regional Emission inventory in ASia (REAS) version 2. *Atmospheric Chemistry and Physics*, *13*(21), 11019–11058. https://doi.org/10.5194/acp-13-11019-2013

Kusaka, H., & Kimura, F. (2004). Coupling a single-layer urban canopy model with a simple atmospheric model: impact on urban heat island simulation for an idealized case. *Journal of the Meteorological Society of Japan*, *82*(1), 67–80. https://doi.org/10.2151/jmsj.82.67

Kuze, A., Suto, H., Nakajima, M., & Hamazaki, T. (2009). Thermal and near infrared sensor for carbon observation Fourier-transform spectrometer on the Greenhouse Gases Observing Satellite for greenhouse gases monitoring. *Applied Optics*, *48*(35), 6716. https://doi.org/10.1364/AO.48.006716

Lac, C., Donnelly, R. P., Masson, V., Pal, S., Riette, S., Donier, S., … Xueref-Remy, I. (2013). CO_2 dispersion modelling over Paris region within the CO_2-MEGAPARIS project. *Atmospheric Chemistry and Physics*, *13*(9), 4941–4961. https://doi.org/10.5194/acp-13-4941-2013

Lauvaux, T., & Davis, K. J. (2014). Planetary boundary layer errors in mesoscale inversions of column-

integrated CO_2 measurements. *Journal of Geophysical Research: Atmospheres*, *119*(2), 490–508. https://doi.org/10.1002/2013JD020175Lauvaux, T., Miles, N. L., Deng, A., Richardson, S. J., Cambaliza, M. O., Davis, K. J., … Wu, K. (2016). High-resolution atmospheric inversion of urban CO_2 emissions during the dormant season of the Indianapolis Flux Experiment (INFLUX). *Journal of Geophysical Research: Atmospheres*, *121*(10), 5213–5236. https://doi.org/10.1002/2015JD024473

Lauvaux, T., Schuh, A. E., Uliasz, M., Richardson, S., Miles, N., Andrews, A. E., … Davis, K. J. (2012). Constraining the CO_2 budget of the corn belt: exploring uncertainties from the assumptions in a mesoscale inverse system. *Atmospheric Chemistry and Physics*, *12*(1), 337–354. https://doi.org/10.5194/acp-12-337-2012

Le Quéré, C., Andrew, R., Friedlingstein, P., Sitch, S., Hauck, J., Pongratz, J., … Zheng, B. (2018). Global Carbon Budget 2018. *Earth System Science Data*, *10*(4), 2141–2194. https://doi.org/10.5194/essd-10-2141-2018

Lin, J. C., & Gerbig, C. (2005). Accounting for the effect of transport errors on tracer inversions. *Geophysical Research Letters*, *32*(1), L01802. https://doi.org/10.1029/2004GL021127

Mandrake, L., O' Dell, C., Wunch, D., Wennberg, P. O., Fisher, B., Osterman, G. B., & A., E. (2015). OCO-2 XCO_2 warn level, bias correction, and lite file product description. *Version1*. Pasadena, California.

Martilli, A., Clappier, A., & Rotach, M. W. (2002). An urban surface exchange parameterisation for mesoscale models. *Boundary-Layer Meteorology*, *104*(2), 261–304. https://doi.org/10.1023/A:1016099921195

McKain, K., Wofsy, S. C., Nehrkorn, T., Eluszkiewicz, J., Ehleringer, J. R., & Stephens, B. B. (2012). Assessment of ground-based atmospheric observations for verification of greenhouse gas emissions from an urban region. *Proceedings of the National Academy of Sciences*, *109*(22),

8423–8428. https://doi.org/10.1073/pnas.1116645109

McPherson, E. G., Simpson, J. R., Xiao, Q., & Wu, C. (2008). *Los Angeles 1-million tree canopy cover assessment. general technical report PSW-GTR-207*. Albany, CA.

Miles, N. L., Richardson, S. J., Lauvaux, T., Davis, K. J., Balashov, N. V., Deng, A., … Shepson, P. B. (2017). Quantification of urban atmospheric boundary layer greenhouse gas dry mole fraction enhancements in the dormant season: Results from the Indianapolis Flux Experiment (INFLUX). *Elem Sci Anth*, *5*, 27. https://doi.org/10.1525/elementa.127

Miller, J. B., Lehman, S., Verhulst, K. R., Yadav, V., Miller, C., Duren, R., … Sloop, C. (2017). Unexpected and Significant Biospheric CO_2 Fluxes in the Los Angeles Basin Indicated by Atmospheric Radiocarbon ($14CO_2$). In *45th Global Monitoring Annual Conference*. Boulder, Colorado, USA.

Miller, S. M., Hayek, M. N., Andrews, A. E., Fung, I., & Liu, J. (2015). Biases in atmospheric CO_2 estimates from correlated meteorology modeling errors. *Atmospheric Chemistry and Physics*, *15*(5), 2903–2914. https://doi.org/10.5194/acp-15-2903-2015

Morino, I., Uchino, O., Inoue, M., Yoshida, Y., Yokota, T., Wennberg, P. O., … Rettinger, M. (2011). Preliminary validation of column-averaged volume mixing ratios of carbon dioxide and methane retrieved from GOSAT short-wavelength infrared spectra. *Atmospheric Measurement Techniques*, *4*(6), 1061–1076. https://doi.org/10.5194/amt-4-1061-2011

Moore, B., Crowell, S. M. R., Rayner, P. J., Kumer, J., O'Dell, C. W., O'Brien, D., … Lemen, J. (2018). The Potential of the Geostationary Carbon Cycle Observatory (GeoCarb) to provide multi-scale constraints on the carbon cycle in the Americas. *Frontiers in Environmental Science*, *6*(OCT), 1–13. https://doi.org/10.3389/fenvs.2018.00109

Nakanishi, M., & Niino, H. (2004). An improved Mellor–Yamada level-3 model with condensation physics: its design and verification. *Boundary-Layer Meteorology*, *112*(1), 1–31.

https://doi.org/10.1023/B:BOUN.0000020164.04146.98

Nassar, R., Hill, T. G., McLinden, C. A., Wunch, D., Jones, D. B. A., & Crisp, D. (2017). Quantifying CO_2 Emissions From Individual Power Plants From Space. *Geophysical Research Letters*, *44*(19), 10,045-10,053. https://doi.org/10.1002/2017GL074702

Nassar, R., Napier-Linton, L., Gurney, K. R., Andres, R. J., Oda, T., Vogel, F. R., & Deng, F. (2013). Improving the temporal and spatial distribution of CO_2 emissions from global fossil fuel emission data sets. *Journal of Geophysical Research: Atmospheres*, *118*(2), 917–933. https://doi.org/10.1029/2012JD018196

O'Dell, C. W., Connor, B., Bösch, H., O'Brien, D., Frankenberg, C., Castano, R., … Wunch, D. (2012). The ACOS CO_2 retrieval algorithm – Part 1: Description and validation against synthetic observations. *Atmospheric Measurement Techniques*, *5*(1), 99–121. https://doi.org/10.5194/amt-5-99-2012

Oda, T., Lauvaux, T., Lu, D., Rao, P., Miles, N. L., Richardson, S. J., & Gurney, K. R. (2017). On the impact of granularity of space-based urban CO_2 emissions in urban atmospheric inversions: A case study for Indianapolis, IN. *Elem Sci Anth*, *5*, 28. https://doi.org/10.1525/elementa.146

Oda, T., & Maksyutov, S. (2011). A very high-resolution (1 km×1 km) global fossil fuel CO_2 emission inventory derived using a point source database and satellite observations of nighttime lights. *Atmospheric Chemistry and Physics*, *11*(2), 543–556. https://doi.org/10.5194/acp-11-543-2011

Oda T., & Maksyutov, S. (2015). ODIAC Fossil Fuel CO_2 Emissions Dataset (ODIAC v1.7), Center for Global Environmental Research, National InFstitute for Environmental Studies, Downloaded from http://db.cger.nies.go.jp/dataset/ODIAC/.

Oda, T., Maksyutov, S., & Andres, R. J. (2018). The Open-source Data Inventory for Anthropogenic CO_2, version 2016 (ODIAC2016): a global monthly fossil fuel CO_2 gridded emissions data product for tracer transport simulations and surface flux inversions. *Earth System Science Data*,

10(1), 87–107. https://doi.org/10.5194/essd-10-87-2018

Oda, T., Ott, L., Topylko, P., Halushchak, M., Bun, R., Lesiv, M., … Horabik-Pyzel, J. (2015). Uncertainty associated with fossil fuel carbon dioxide (CO_2) gridded emission datasets. In *4th International Workshop on Uncertainty in Atmospheric Emissions* (pp. 124–129). 7-9 October 2015, Krakow, Poland: Systems Research Institute, Polish Academy of Sciences.

Oda, T., Bun, R., Kinakh, V., Topylko, P., Halushchak, M., Marland, G., … Horabik-Pyzel, J. (2019). Errors and uncertainties in a gridded carbon dioxide emissions inventory. *Mitigation and Adaptation Strategies for Global Change*, 1007–1050. https://doi.org/10.1007/s11027-019-09877-2

Pacala, S. W., Breidenich, C., Brewer, P. G., Fung, I., Gunson, M. R., Heddle, G., … Wofsy, S. C. (2010). *Verifying greenhouse gas emissions: methods to support international climate agreements*. Washington, D.C.: National Academies Press. https://doi.org/10.17226/12883

Raciti, S. M., Hutyra, L. R., Rao, P., & Finzi, A. C. (2012). Inconsistent definitions of "urban" result in different conclusions about the size of urban carbon and nitrogen stocks. *Ecological Applications*, *22*(3), 1015–1035. https://doi.org/10.1890/11-1250.1

Reuter, M., Buchwitz, M., Hilboll, A., Richter, A., Schneising, O., Hilker, M., … Burrows, J. P. (2014). Decreasing emissions of NOx relative to CO_2 in East Asia inferred from satellite observations. *Nature Geoscience*, *7*(11), 792–795. https://doi.org/10.1038/ngeo2257

Rotty, R. M. (1983). Distribution of and changes in industrial carbon dioxide production. *Journal of Geophysical Research*, *88*(C2), 1301. https://doi.org/10.1029/JC088iC02p01301

Rypdal, K., & Winiwarter, W. (2001). Uncertainties in greenhouse gas emission inventories — evaluation, comparability and implications. *Environmental Science & Policy*, *4*(2–3), 107–116. https://doi.org/10.1016/S1462-9011(00)00113-1

Satterthwaite, D. (2008). Cities' contribution to global warming: notes on the allocation of greenhouse

gas emissions. *Environment and Urbanization*, *20*(2), 539–549. https://doi.org/10.1177/0956247808096127

Schneising, O., Buchwitz, M., Burrows, J. P., Bovensmann, H., Reuter, M., Notholt, J., … Warneke, T. (2008). Three years of greenhouse gas column-averaged dry air mole fractions retrieved from satellite – Part 1: Carbon dioxide. *Atmospheric Chemistry and Physics*, *8*(14), 3827–3853. https://doi.org/10.5194/acp-8-3827-2008

Schneising, O., Heymann, J., Buchwitz, M., Reuter, M., Bovensmann, H., & Burrows, J. P. (2013). Anthropogenic carbon dioxide source areas observed from space: assessment of regional enhancements and trends. *Atmospheric Chemistry and Physics*, *13*(5), 2445–2454. https://doi.org/10.5194/acp-13-2445-2013

Schwandner, F. M., Gunson, M. R., Miller, C. E., Carn, S. A., Eldering, A., Krings, T., … Podolske, J. R. (2017). Spaceborne detection of localized carbon dioxide sources. *Science*, *358*(6360). https://doi.org/10.1126/science.aam5782

Silva, S. J., Arellano, A. F., & Worden, H. M. (2013). Toward anthropogenic combustion emission constraints from space-based analysis of urban CO_2/CO sensitivity. *Geophysical Research Letters*, *40*(18), 4971–4976. https://doi.org/10.1002/grl.50954

Skamarock, W. C., Klemp, J. B., Dudhia, J., Gill, D. O., & Barker, D. M. (2008). *A description of the Advanced Research WRF Version 3*. Boulder, Colorado, USA.

Staufer, J., Broquet, G., Bréon, F. M., Puygrenier, V., Chevallier, F., Xueref-Rémy, I., … Ciais, P. (2016). The first 1-year-long estimate of the Paris region fossil fuel CO2 emissions based on atmospheric inversion. *Atmospheric Chemistry and Physics*, *16*(22), 14703–14726. https://doi.org/10.5194/acp-16-14703-2016

Super, I., Denier van der Gon, H. A. C., Visschedijk, A. J. H., Moerman, M. M., Chen, H., van der Molen, M. K., & Peters, W. (2017). Interpreting continuous in-situ observations of carbon dioxide

and carbon monoxide in the urban port area of Rotterdam. *Atmospheric Pollution Research*, *8*(1), 174–187. https://doi.org/10.1016/j.apr.2016.08.008

Taylor, T. E., O'Dell, C. W., Frankenberg, C., Partain, P. T., Cronk, H. Q., Savtchenko, A., … Gunson, M. R. (2016). Orbiting Carbon Observatory-2 (OCO-2) cloud screening algorithms: Validation against collocated MODIS and CALIOP data. *Atmospheric Measurement Techniques*, *9*(3), 973–989. https://doi.org/10.5194/amt-9-973-2016

Turnbull, J. C., Karion, A., Fischer, M. L., Faloona, I., Guilderson, T., Lehman, S. J., … Tans, P. P. (2011). Assessment of fossil fuel carbon dioxide and other anthropogenic trace gas emissions from airborne measurements over Sacramento, California in spring 2009. *Atmospheric Chemistry and Physics*, *11*(2), 705–721. https://doi.org/10.5194/acp-11-705-2011

Turnbull, J. C., Keller, E. D., Norris, M. W., & Wiltshire, R. M. (2016). Independent evaluation of point source fossil fuel CO 2 emissions to better than 10%. *Proceedings of the National Academy of Sciences*, *113*(37), 10287–10291. https://doi.org/10.1073/pnas.1602824113

Turnbull, J. C., Sweeney, C., Karion, A., Newberger, T., Lehman, S. J., Tans, P. P., … Razlivanov, I. (2015). Toward quantification and source sector identification of fossil fuel CO_2 emissions from an urban area: Results from the INFLUX experiment. *Journal of Geophysical Research: Atmospheres*, *120*(1), 292–312. https://doi.org/10.1002/2014JD022555

Turnbull, J. C., Tans, P. P., Lehman, S. J., Baker, D., Conway, T. J., Chung, Y. S., … Zhou, L.-X. (2011). Atmospheric observations of carbon monoxide and fossil fuel CO_2 emissions from East Asia. *Journal of Geophysical Research: Atmospheres*, *116*(D24), n/a-n/a. https://doi.org/10.1029/2011JD016691

UN-Habitat. (2011). *Cities and Climate Change: Global Report on Human Settlements 2011*. London, UK and Washington, DC, USA. https://doi.org/978-92-1-132296-5

UNFCCC. (2015). Action taken by the Conference of the Parties at its twenty-first session. In *Report of*

the Conference of the Parties on its twenty-first session. Paris, France: United Nations Framework Convention on Climate Change.

United Nations. (1998). *Kyoto protocol to the United Nations framework convention on climate change*.

Vahmani, P., & Ban-Weiss, G. A. (2016). Impact of remotely sensed albedo and vegetation fraction on simulation of urban climate in WRF-urban canopy model: A case study of the urban heat island in Los Angeles. *Journal of Geophysical Research: Atmospheres*, *121*(4), 1511–1531. https://doi.org/10.1002/2015JD023718

van der Gon, H. D., Beevers, S., D'Allura, A., Finardi, S., Honoré, C., Kuenen, J., … Visschedijk, A. (2011). Discrepancies Between Top-Down and Bottom-Up Emission Inventories of Megacities: The Causes and Relevance for Modeling Concentrations and Exposure. In *Steyn D., Trini Castelli S. (eds) Air Pollution Modeling and its Application XXI. NATO Science for Peace and Security Series C: Environmental Security* (pp. 199–204). Dordrecht: Springer. https://doi.org/10.1007/978-94-007-1359-8_34

Verhulst, K. R., Karion, A., Kim, J., Salameh, P. K., Keeling, R. F., Newman, S., … Miller, C. E. (2017). Carbon dioxide and methane measurements from the Los Angeles Megacity Carbon Project – Part 1: calibration, urban enhancements, and uncertainty estimates. *Atmospheric Chemistry and Physics*, *17*(13), 8313–8341. https://doi.org/10.5194/acp-17-8313-2017

Ware, J., Kort, E. A., DeCola, P., & Duren, R. (2016). Aerosol lidar observations of atmospheric mixing in Los Angeles: Climatology and implications for greenhouse gas observations. *Journal of Geophysical Research: Atmospheres*, *121*(16), 9862–9878. https://doi.org/10.1002/2016JD024953

Winker, D. (2016). CALIPSO LID L2 05kmAPro-Prov HDF File - Version3.40 [Data set]. NASA Langley Atmospheric Science Data Center DAAC. https://doi.org/10.5067/caliop/calipso/lid_l2_05kmapro-prov-v3-40

Worden, J. R., Doran, G., Kulawik, S., Eldering, A., Crisp, D., Frankenberg, C., … Bowman, K. (2017).

Evaluation and attribution of OCO-2 XCO_2 uncertainties. *Atmospheric Measurement Techniques*, *10*(7), 2759–2771

Wu, D., Lin, J. C., Oda, T., Ye, X., Lauvaux, T., Yang, E. G., & Kort, E. A. (2018). A Lagrangian approach towards extracting signals of urban CO2 emissions from satellite observations of atmospheric column CO2 (XCO2): X-Stochastic Time-Inverted Lagrangian Transport model ("X-STILT v1.1"). *Geoscientific Model Development Discussions*, *11*, 4843–4871. https://doi.org/10.5194/gmd-2018-123

Wunch, D., Wennberg, P. O., Osterman, G., Fisher, B., Naylor, B., Roehl, C. M., … Eldering, A. (2017). Comparisons of the Orbiting Carbon Observatory-2 (OCO-2) XCO_2 measurements with TCCON. *Atmospheric Measurement Techniques*, *10*(6), 2209–2238. https://doi.org/10.5194/amt-10-2209-2017

Wunch, D., Wennberg, P. O., Toon, G. C., Keppel-Aleks, G., & Yavin, Y. G. (2009). Emissions of greenhouse gases from a North American megacity. *Geophysical Research Letters*, *36*(15), L15810. https://doi.org/10.1029/2009GL039825

Table 1. Summary of the simulations carried out for the selected cities

City type	City/ Metropolitan region	Land cover (% innermost domain)*	Transport error propagation method	Innermost domain size and resolution	Simulation time
Plume city	Riyadh	Barren or sparse (92.2%)	Perturbed plume	201×201 (1 km)	1-16 November 2014 17 December 2014 – 5 January 2015 27-30 January 2015
	Cairo	Barron or sparse (57.4%) Croplands (32.8%)	Perturbed plume	201×201 (1 km)	4-7 October 2014 16-19 March 2015 17-20 May 2015 13-16 July 2015 14-17 August 2015
Basin city	Los Angeles (LA) metropolitan region	Water (45.2%) Open shrublands (34.9%) Barren or sparse (6.1%) Woody savannas (3.6%) Croplands (2.9%)	Ensemble simulation	207×150** (4 km)	3 July – 20 August 2015 6-19 October 2015
Multi-city	Pearl River Delta (PRD) metropolitan region	Water (26.7%) Croplands (26.2%) Evergreen broadleaf (20.0%) Woody savannas (10.1%) Urban (8.6%)	Perturbed plume	240×240 (1.333 km)	12-15 January 2015 1-4 August 2015

*Land cover is based on MODIS IGBP 21-category data. The land cover types accounting for more than 90% of the innermost domain in aggregate are listed.

**The domain of interest for LA is set to 119.0° W~116.3°W, 32.2°N~35.7°N, which is smaller than the innermost domain of simulations.

Table 2. WRF model configurations of the ensemble of simulations conducted for Los Angeles

Ensemble member	**PBL scheme**	**Surface layer scheme**	**Urban Canopy model**
MYJ	MYJ	Eta similarity (Janjić Eta)	None
MYJ_UCM	MYJ	Eta similarity (Janjić Eta)	Noah UCM
MYNN	MYNN	Nakanishi and Niino	None
MYNN_UCM	MYNN	Nakanishi and Niino	Noah UCM
BouLac_BEP	BouLac	Eta similarity (Janjić Eta)	BEP
BouLac_UCM	BouLac	Eta similarity (Janjić Eta)	Noah UCM

Table 3. Inversion results of scaling factors of the whole-city emissions for the selected cities using OCO-2 X_{CO2} data. The scaling factors and their posterior uncertainties are shown for each individual track, as well as for integrating the information from all the selected tracks. Uncertainty components are listed for each track, including the prior uncertainty of scaling factor, and the measurement and transport uncertainties of the integral ffX_{CO2} (the larger value between these two is shown in bold).

City	Date of OCO-2 track	Prior total emission (MtC mo^{-1})	Prior total emission uncertainty (σ_a)	Measurement uncertainty ($\sigma_{measurement}$, units: ppm)	Transport model uncertainty (σ_{model}, units: ppm)	scaling factor (λ) ± posterior uncertainty ($\hat{\sigma}$)	
Riyadh	Dec 27, 2014	3.08	40%	1.34	**2.80**	0.92±0.24	0.85±0.16
	Dec 29, 2014	3.08		1.30	**2.83**	0.83±0.17	
Cairo	Feb 28, 2015	2.52	40%	**1.07**	0.71	0.79±0.15	0.83±0.074
	Mar 18, 2015	2.70		**0.55**	0.31	1.18±0.25	
	May 19, 2015	2.48		**1.18**	0.36	0.95±0.11	
	Jul 15, 2015	2.62		**1.08**	0.16	0.70±0.13	
	Aug 16, 2015	2.61		**0.94**	0.54	0.81±0.10	
Los Angeles	Jul 6, 2015	4.68	20%	1.48	**2.99**	1.00±0.15	1.36±0.074
	Jul 15, 2015	4.68		**2.11**	1.62	1.84±0.16	
	Aug 7, 2015	4.74		1.11	**1.35**	1.17±0.15	
	Aug 16, 2015	4.74		1.93	**3.03**	1.43±0.14	
	Oct 10, 2015	4.49		**1.20**	1.08	1.64±0.15	
	Oct 12, 2015	4.49		1.40	**2.70**	0.66±0.11	

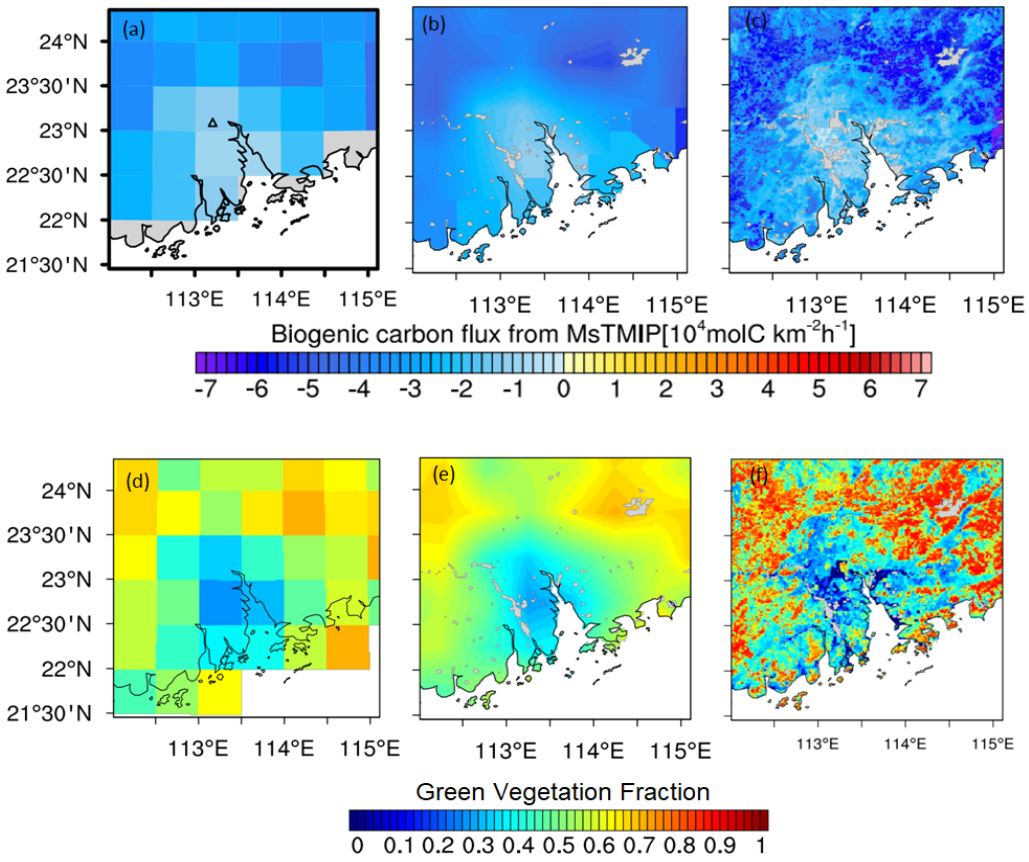

Figure 1. Example of biogenic carbon fluxes (Net Ecosystem Exchange, NEE) downscaling in PRD region. Top panels show the NEE from 3-hourly MsTMIP data at 12:00 LT January 12, 2010 on (a) the original 0.5°×0.5° grid, (b) WRF grid (1.333×1.333 km), derived by bilinear interpolation of original NEE, and (c) WRF grid (1.333×1.333 km), derived by scaling the interpolated NEE. Bottom panels show the green vegetation fraction (GVF) in January on (d) the 0.5°×0.5° grid, (e) WRF grid (1×1 km) by bilinear interpolation of GVF in (d), and (f) WRF grid (1×1 km). See section 2.4.3 for further details.

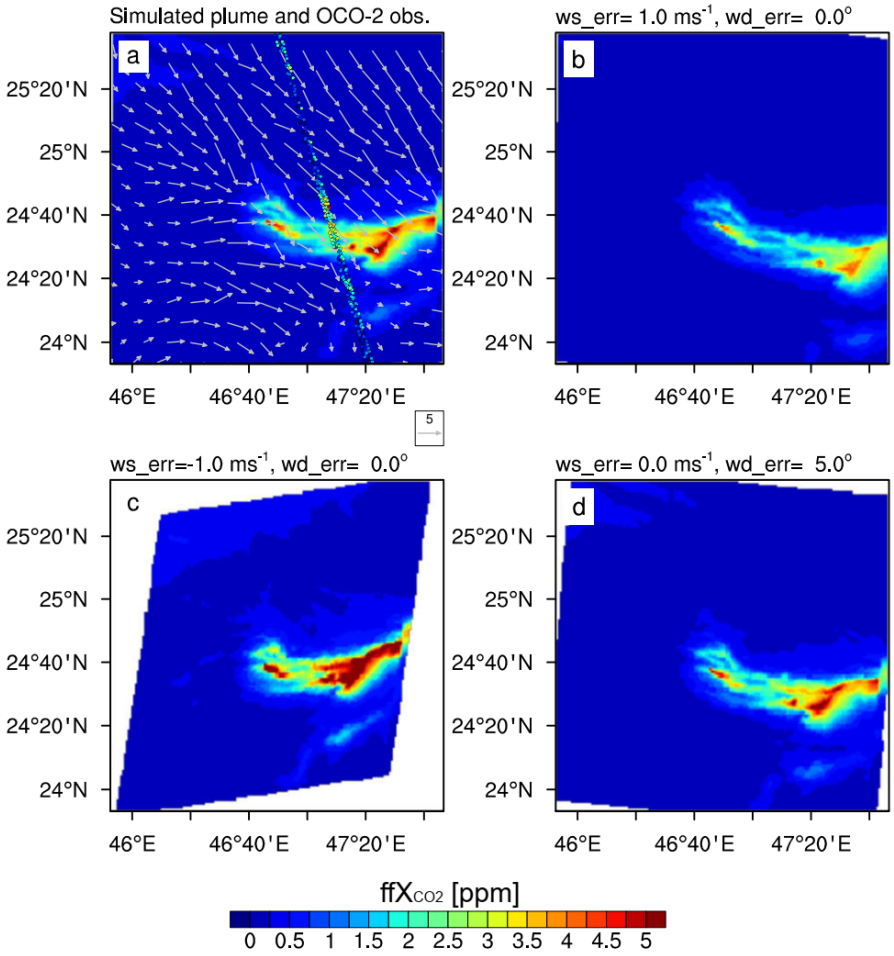

Figure 2. (a) Local ffX_{CO2} derived from OCO-2 data (colored dots) at about 10:00 UTC 29 December 2014 by subtracting the background concentration and the simulated ffX_{CO2} enhancement (color shading) using ODIAC emissions, which is the truth in the OSSEs. Panel (b) and (c) show the rescaled plumes of panel (a) with wind speed error of 1.0 ms^{-1} and -1.0 m s^{-1}. Panel (d) shows the rescaled plume with wind direction error of 5.0°.

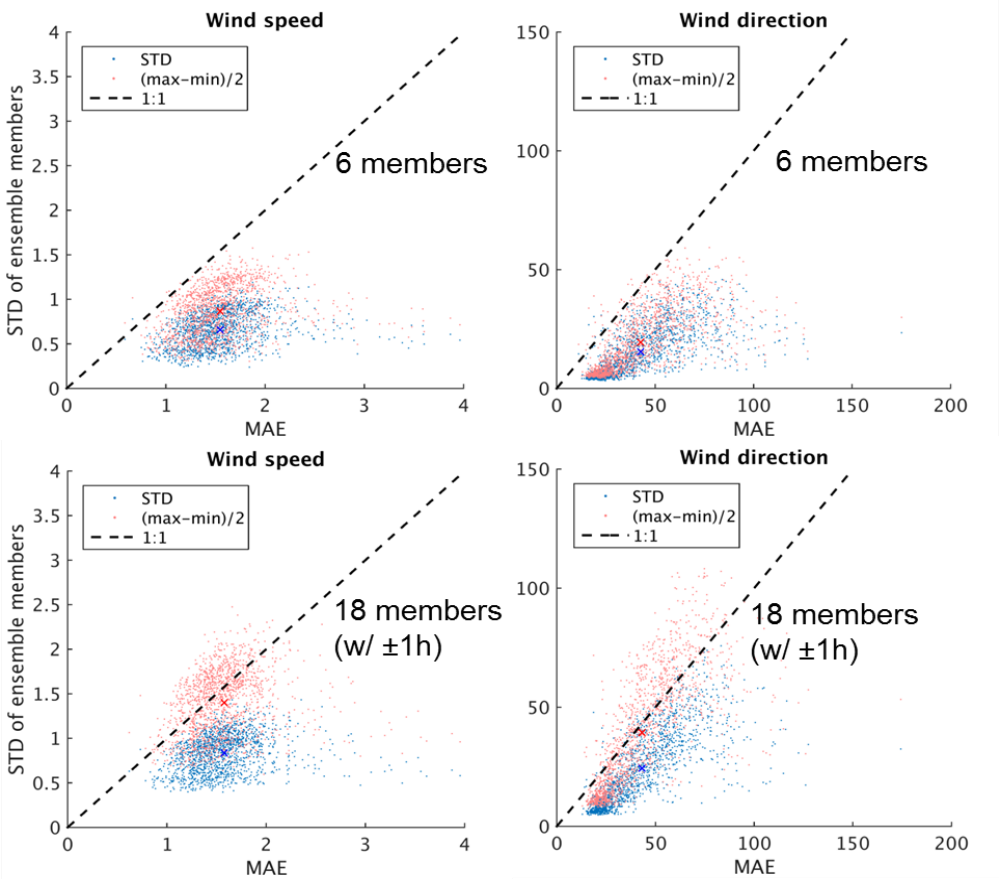

Figure 3. Comparison of the modeling uncertainty and mean absolute error (MAE) of 10-m wind speeds and wind directions over 43 surface sites located in the 1.333-km resolution domain for LA. The modeling random uncertainty is calculated as the standard deviation (STD, blue scatters) and semi-full range of the modeling results, i.e. half of the difference between maximum and minimum values among the ensemble members (red scatters). The top two panels show results for the original six members, and the bottom two panels for the 18 members with modeling results at ±1 h included. The red and blue crosses in each panel stand for average points of the scatters in the corresponding colors.

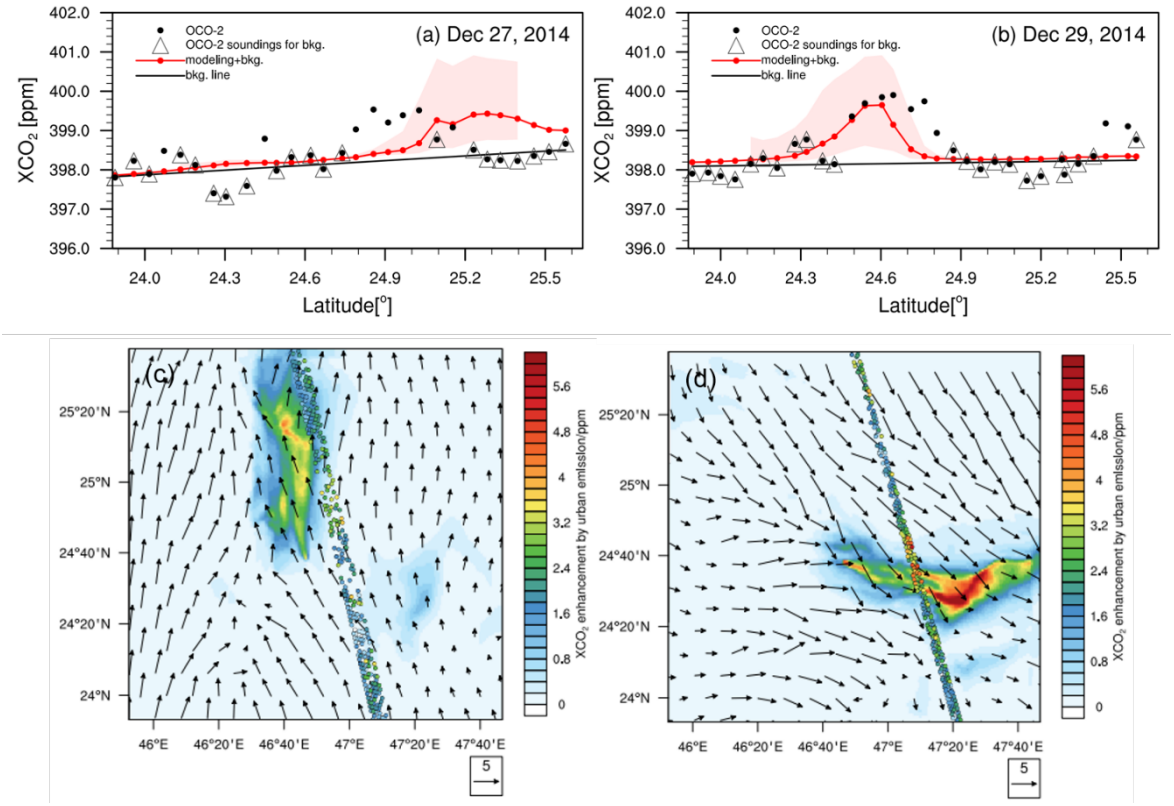

Figure 4. Comparisons of modeled and observed ffX_{CO2} enhancements by the OCO-2 data on 27and 29 December 2014 at about 10:00 UTC over Riyadh. Panels (a) and (b) show the OCO-2 X_{CO2} (black dots) and simulated X_{CO2} (red dotted line, sum of ffX_{CO2} and the background concentrations) along the two tracks. The OCO-2 retrievals are filtered with Quality Flag (QF=0) and are 1-s averaged. The blank triangles represent the data used for the derivation of background concentrations (black solid line) by linear regression with these data versus latitude. The uncertainty in the simulated ffX_{CO2} related to transport model errors are shown by the light red shading. Panels (c) and (d) show the simulated ffX_{CO2} and the observed ffX_{CO2} obtained from the OCO-2 data, filtered with QF=0 only. The background X_{CO2} concentrations have been subtracted. The vectors represent 10-m wind with the reference vector standing for the wind speed of 5 m s^{-1}.

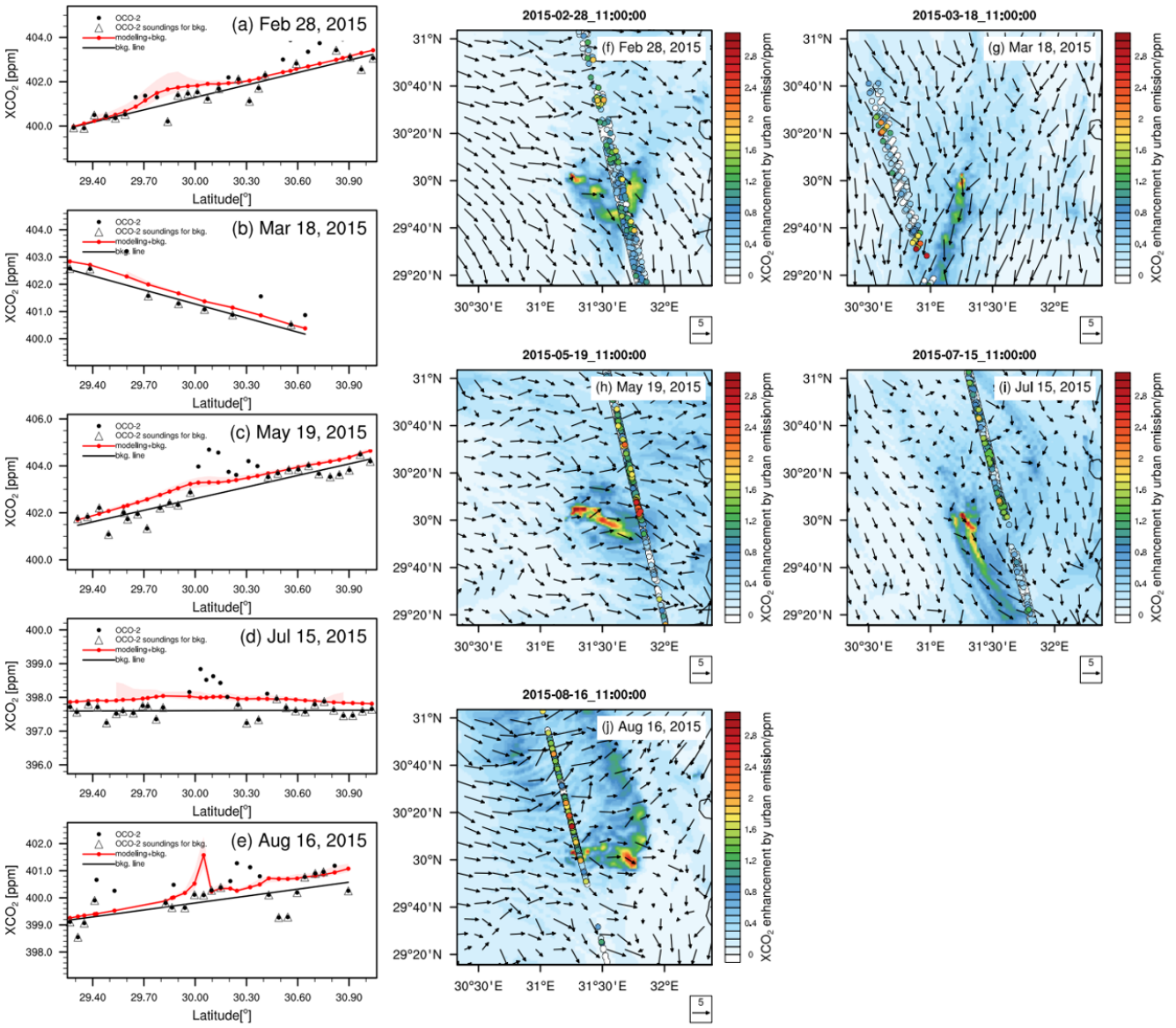

Figure 5. Similar to Fig. 4, but for the OCO-2 tracks over Cairo on (a and f) 28 February, (b and g) 18 March, (c and h) 19 May (d and i) 15 July, and (e and j) 16 August 2015 at about 11:00 UTC.

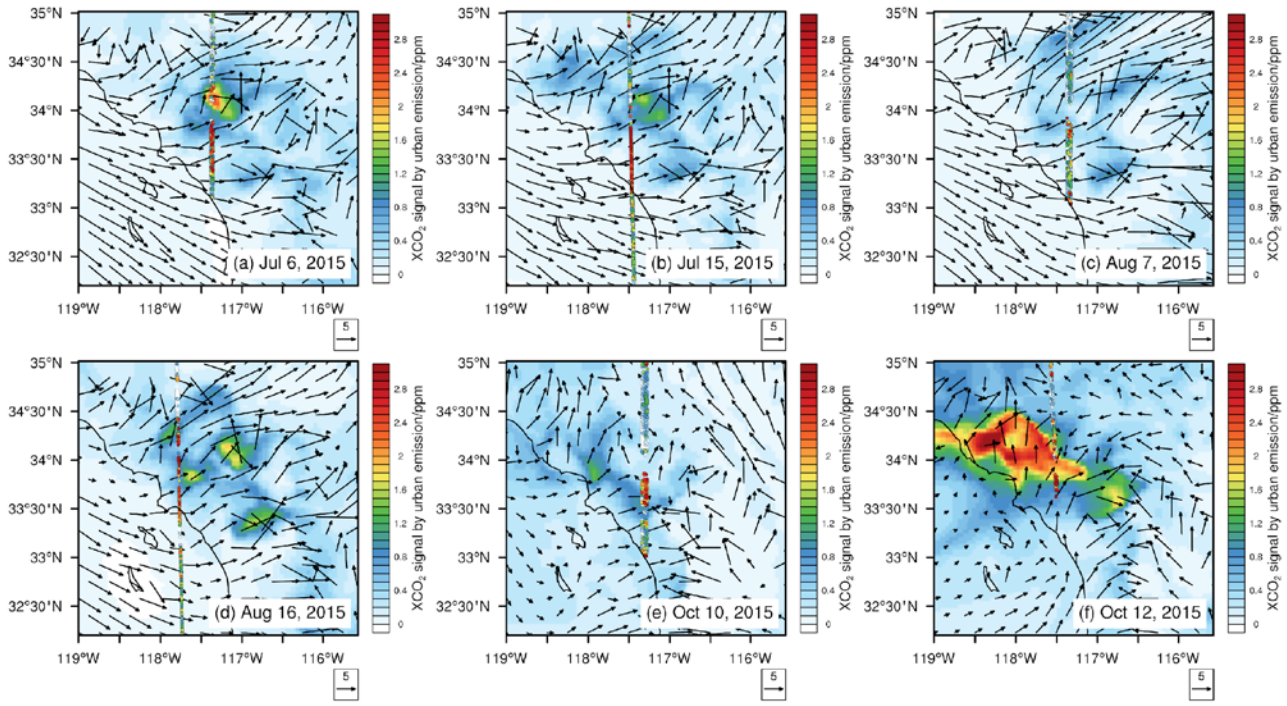

Figure 6. Comparisons of the simulated ffX_{CO2} (color shading) and observed ffX_{CO2} enhancements (colored dots, background concentration subtracted) derived from the OCO-2 data collected at about 21:00 UTC over LA. The observation dates are labeled in each panel. The OCO-2 data are filtered by quality flag of zero (QF=0). The vectors represent 10-m wind, with the reference vector standing for the wind speed of 5 m s^{-1}.

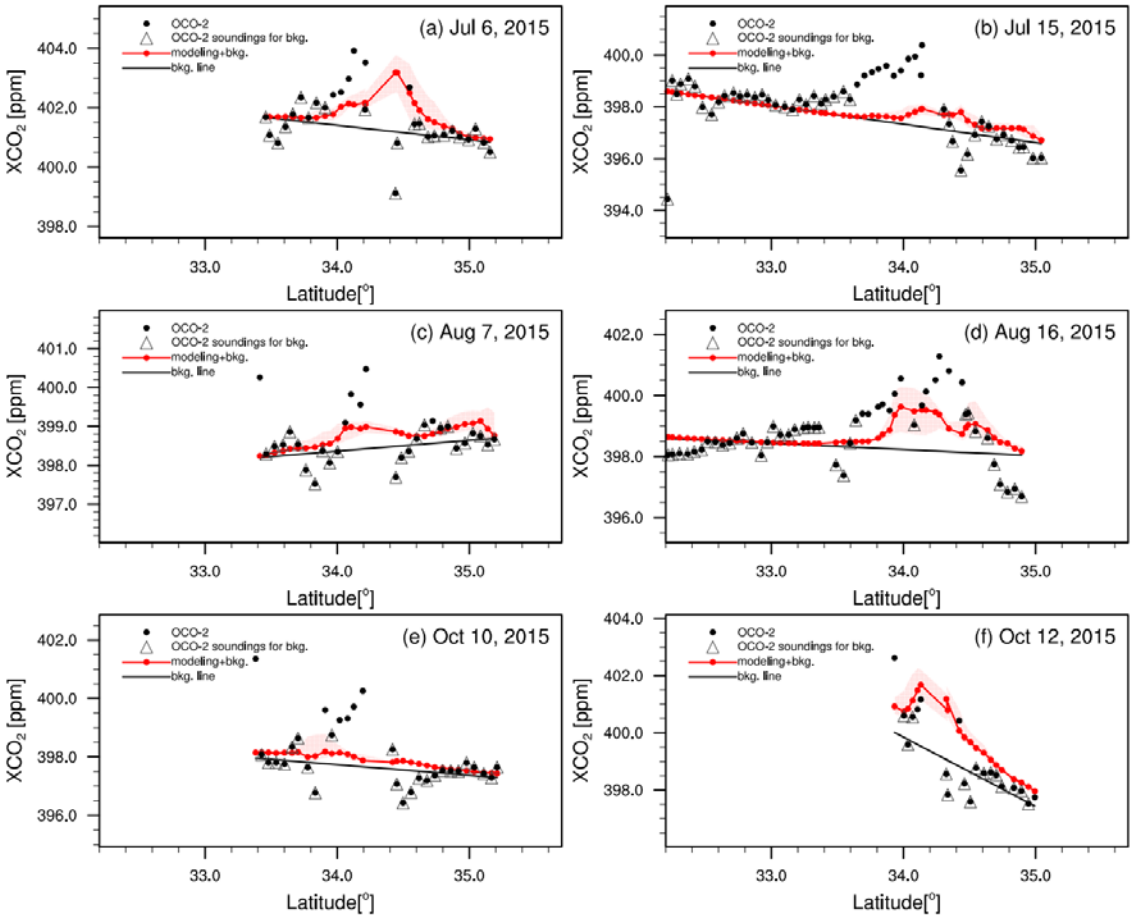

Figure 7. Similar to Figs. 4 (a, b), but for OCO-2 X_{CO2} measurements over LA and the corresponding simulated results at about 21:00 UTC on (a) July 6, (b) July 15, (c) August 7, (d) August 16, (e) October 10, and (f) October 12, 2015.

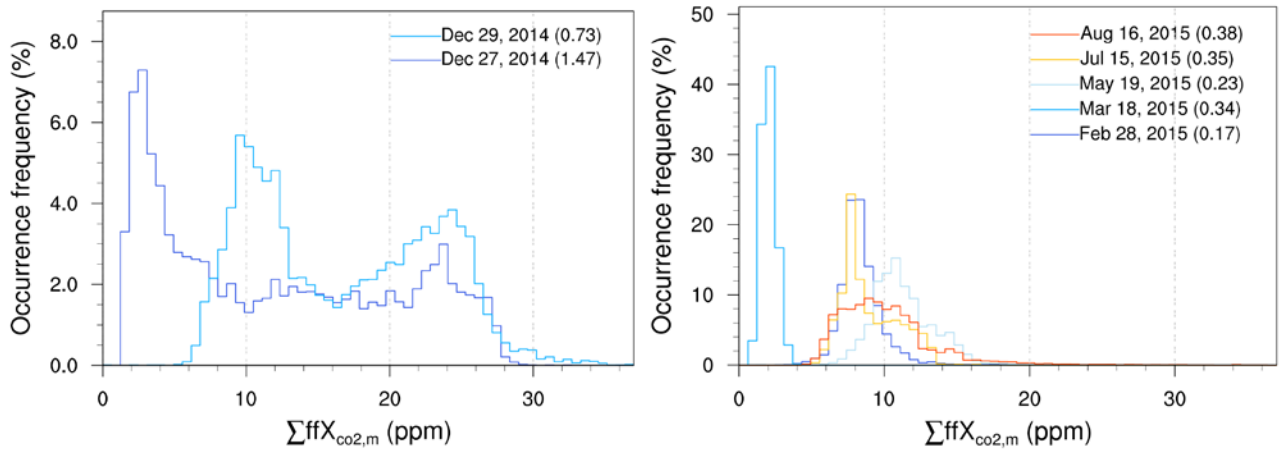

Figure 8. Probability distributions of the modeled integral ffX_{CO2} enhancements ($ffX_{CO2,\ m}$) for the OCO-2 tracks on 27 and 29 December 2014 over Riyadh (left) and 28 February, 28 March, 19 May, 15 July, and 16 August 2015 over Cairo (right). The total number of samples is 10^4 for each track. The distributions represent the uncertainty related to random transport model errors in wind speed and wind direction. Note that the y-axis limits of the two plots are different. The numbers in the parentheses are the ratios of the interquartile range ($q_3 - q_1$) and the median (q_2).

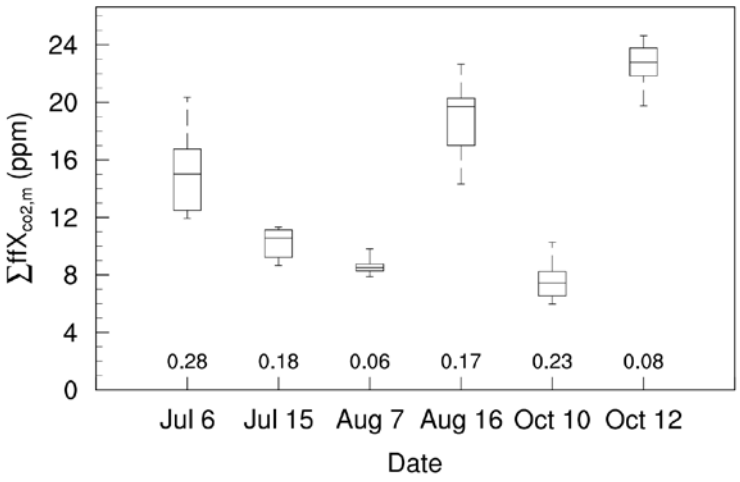

Figure 9. Box plot of the modeled integral ffX_{CO2} enhancements ($ffX_{CO2,\,m}$) for the selected OCO-2 tracks over LA on the dates labeled at the x-axis. For each box, the central line indicates the median (q_2), and the bottom and top edges of the box indicate the 25th and 75th percentiles (q_1 and q_3), respectively. The whiskers extend to the maximum and the minimum. The numbers are the ratios of the interquartile range ($q_3 - q_1$) versus the median (q_2).

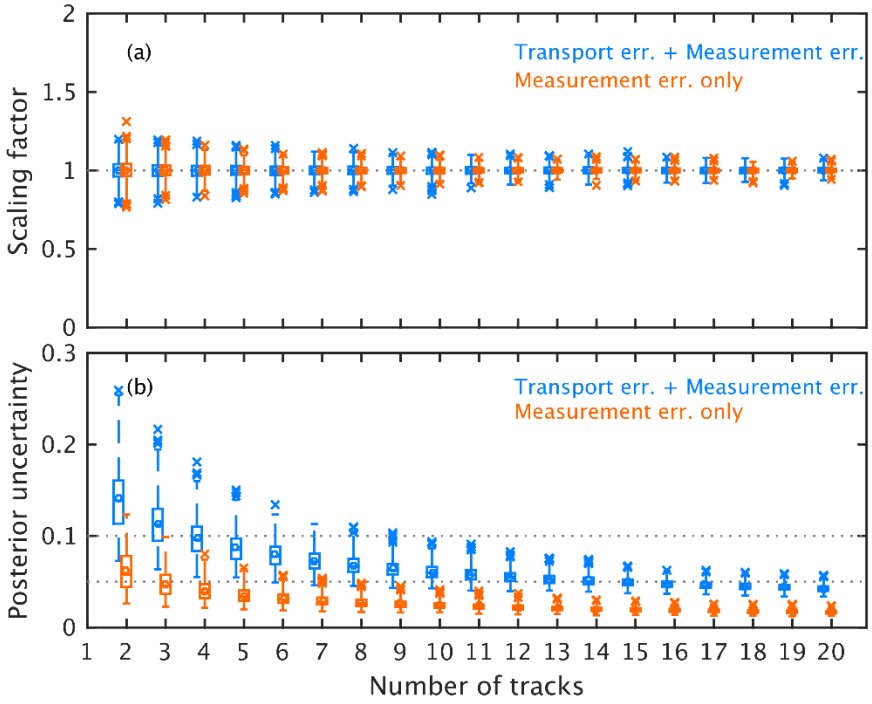

Figure 10. Box plot of the inverse estimates of (a) whole-city emission scaling factor and (b) the posterior uncertainty for Riyadh, derived by the OSSE for different number of OCO-2 tracks (N). The number of repetition times of inversion with each specified value of N is 10^3. For each box, the central line indicates the median, the circle represents the average, and the bottom and top edges of the box indicate the 25th and 75th percentiles (q_1 and q_3), respectively. The outliers are plotted with "x", which are greater than $q_3 + 2\times (q_3 - q_1)$ or less than $q_1 - 2\times (q_3 - q_1)$. The whiskers extend to the most extreme value that is not an outlier.

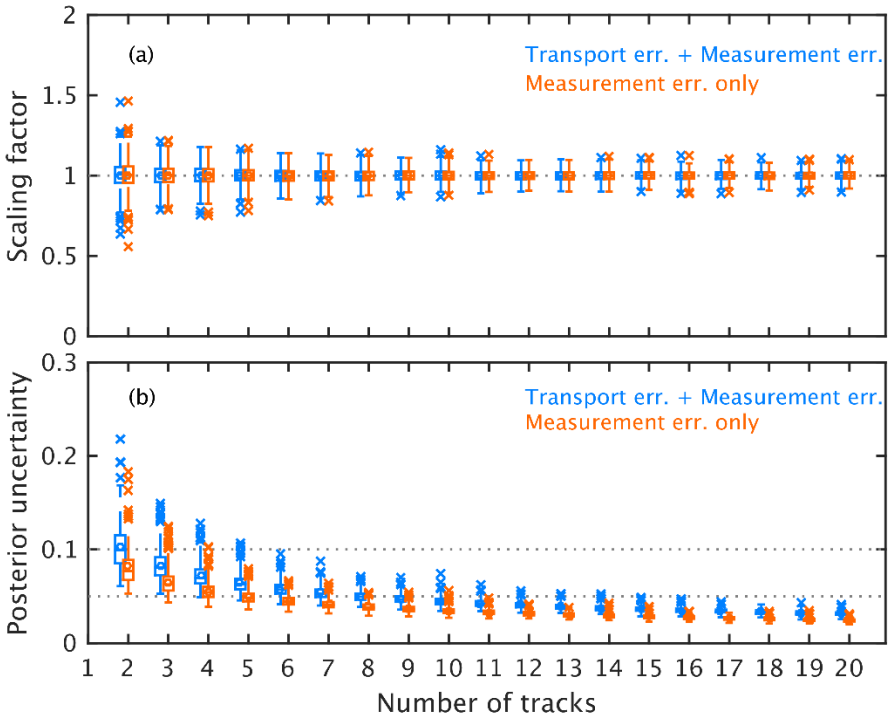

Figure 11. Similar to Fig. 10, but for the OSSE results for Cairo.

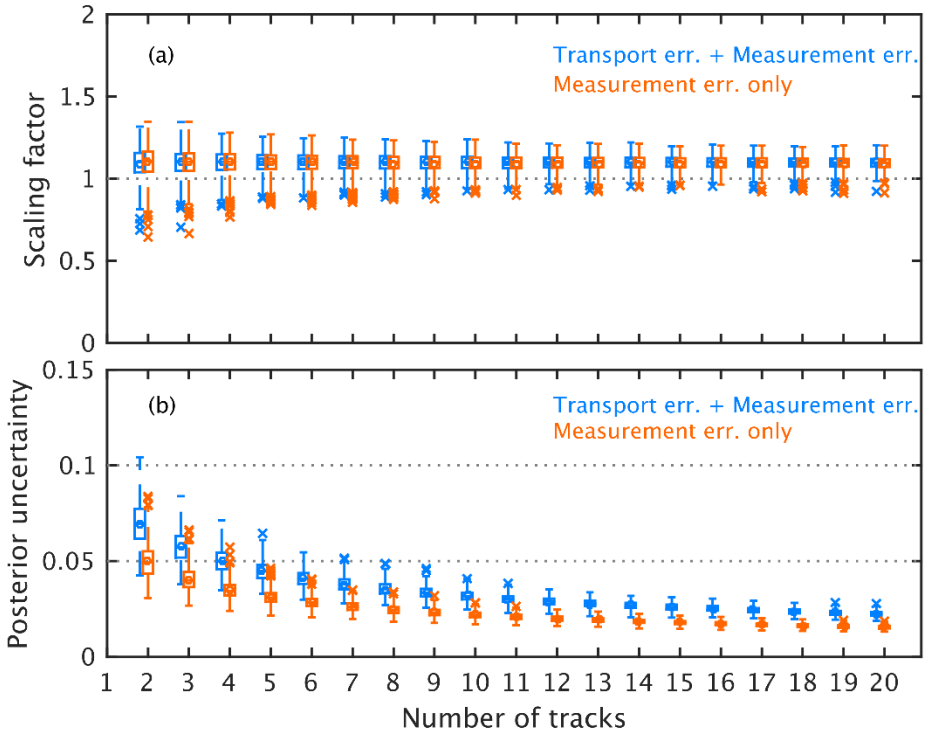

Figure 12. Similar to Fig. 10, but presents the OSSE results for LA.

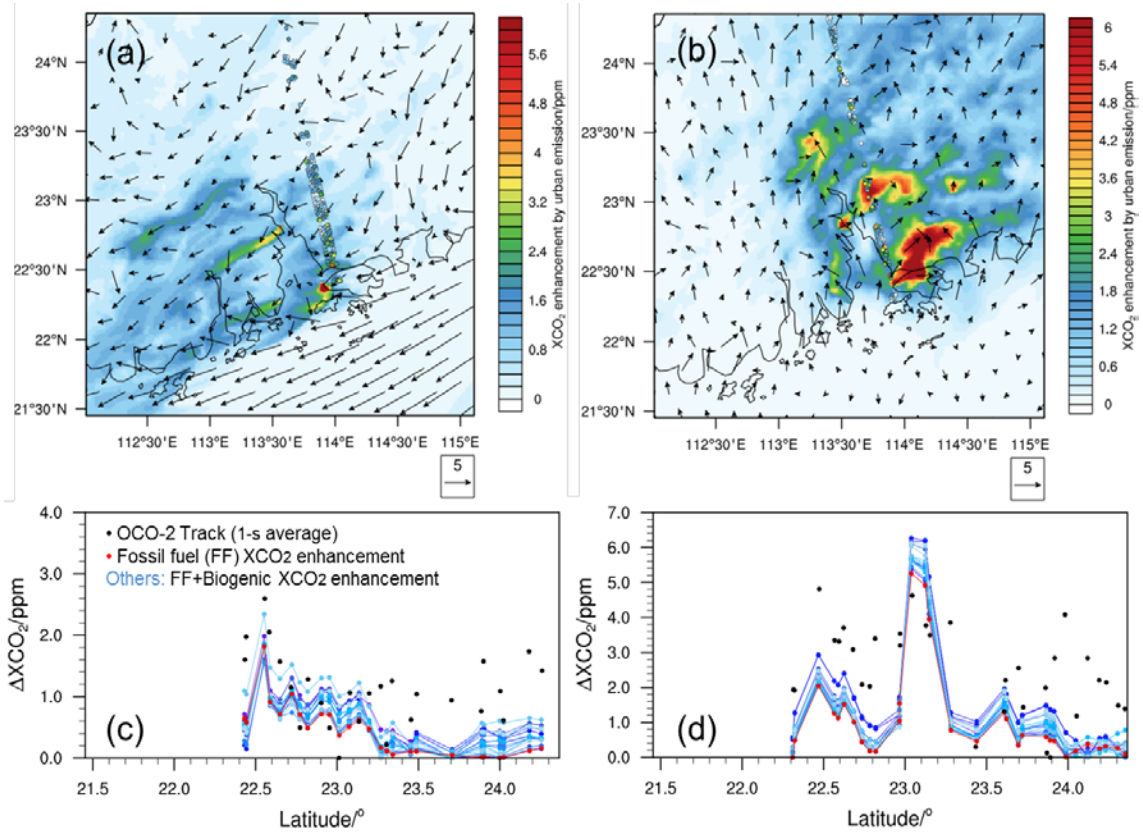

Figure 13. Simulated ffX_{CO2} over the PRD region and the 10-m wind vectors in the 1.333-km resolution domain at (a) 05:00 UTC January 15, 2015, and (b) 05:00 UTC August 4, 2015. The reference vector stands for wind speed of 5 ms^{-1}. The colored dots represent the OCO-2 data at about 05:00 UTC over this domain, filtered with quality flag of zero (QF=0). The background has been subtracted from the OCO-2 data. The black dots in (c) and (d) show the 1-s average observations in the two tracks, with the modeled ffX_{CO2} and ΔX_{CO2} (owing to both fossil fuel and biogenic fluxes) represented by the red and blue dotted lines, respectively. The bunch of blue lines represent the results using NEE from the 15 biospheric models.

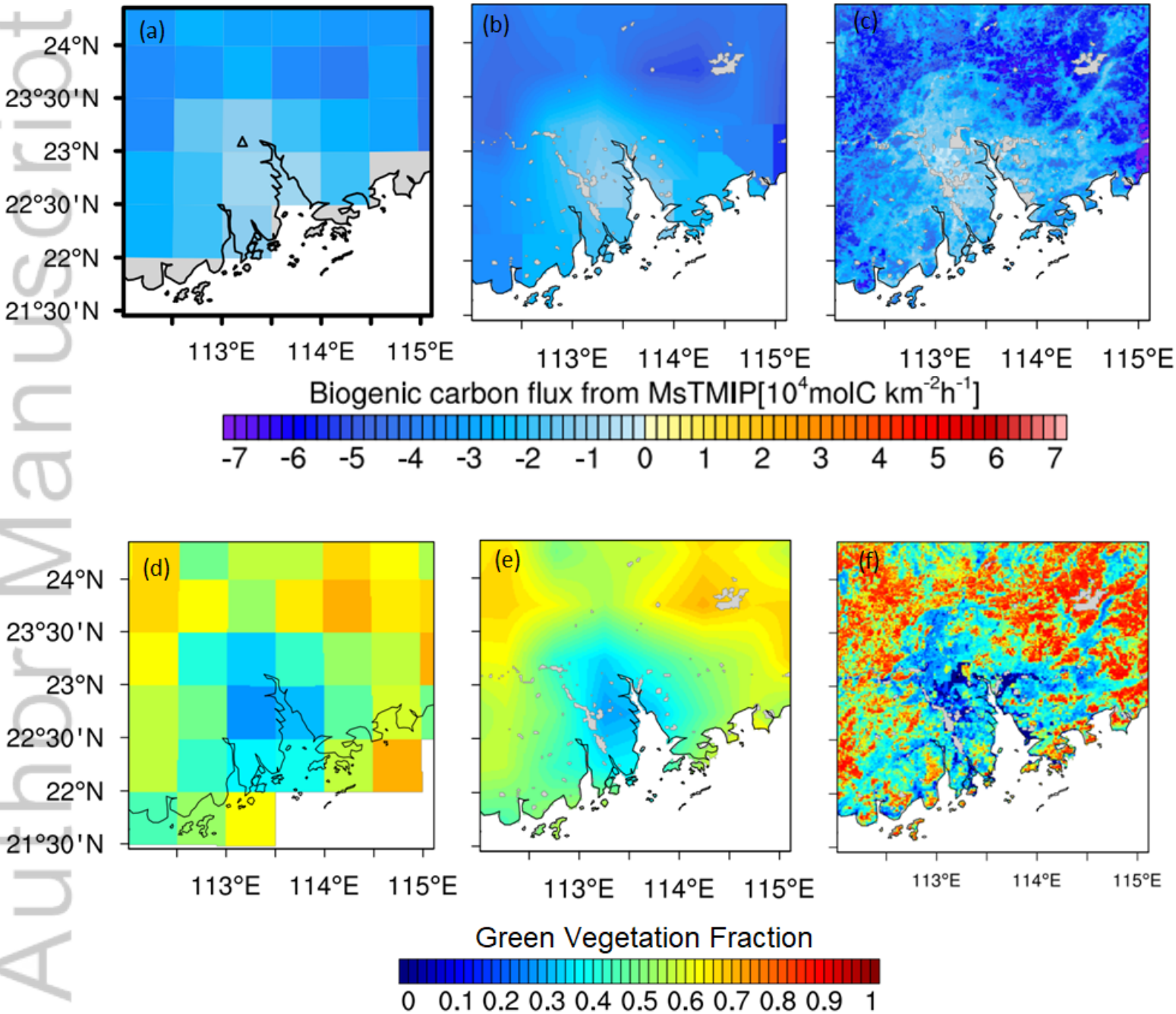

2019JD030528-f01-z-.png

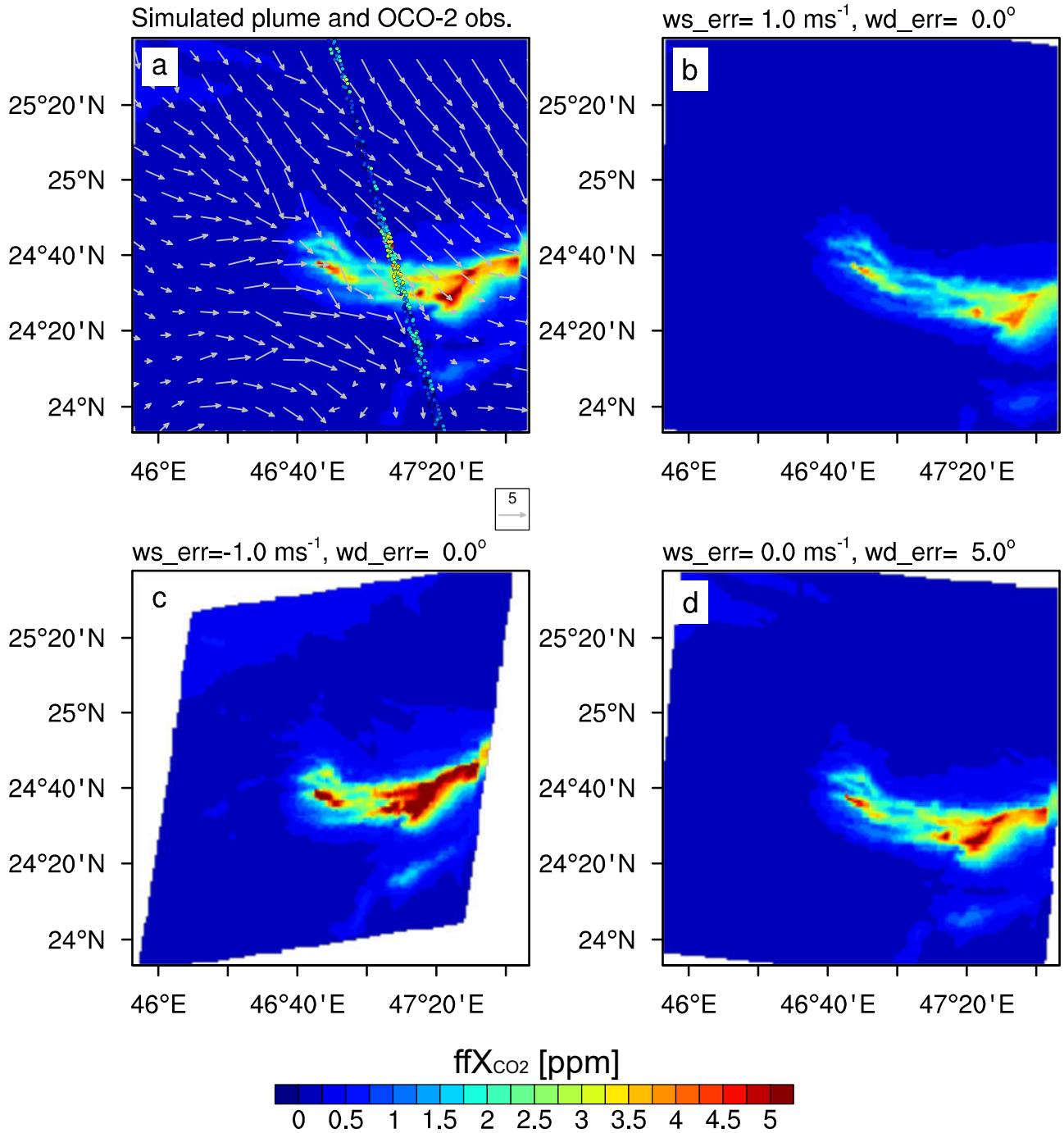

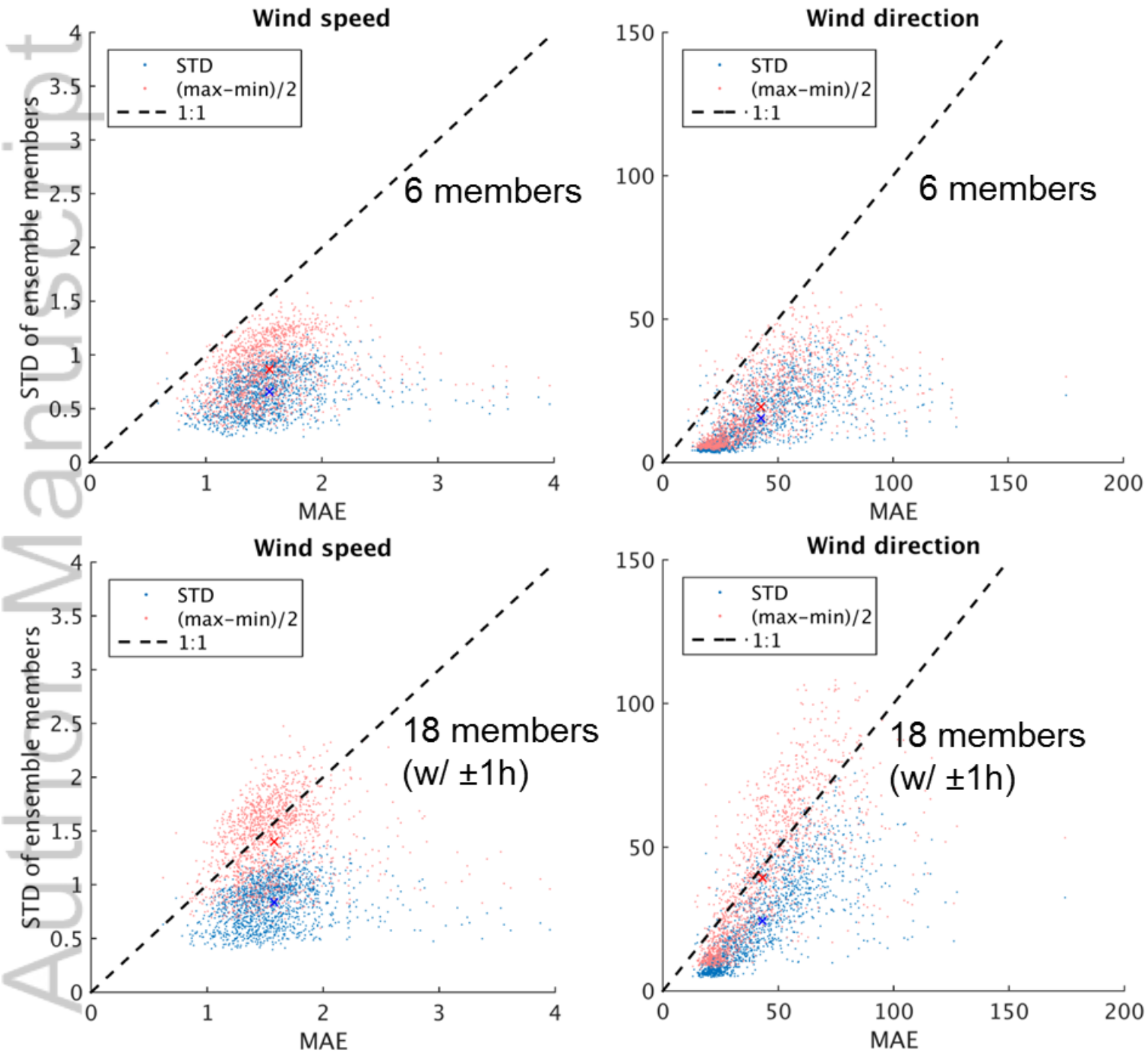

2019JD030528-f03-z-.png

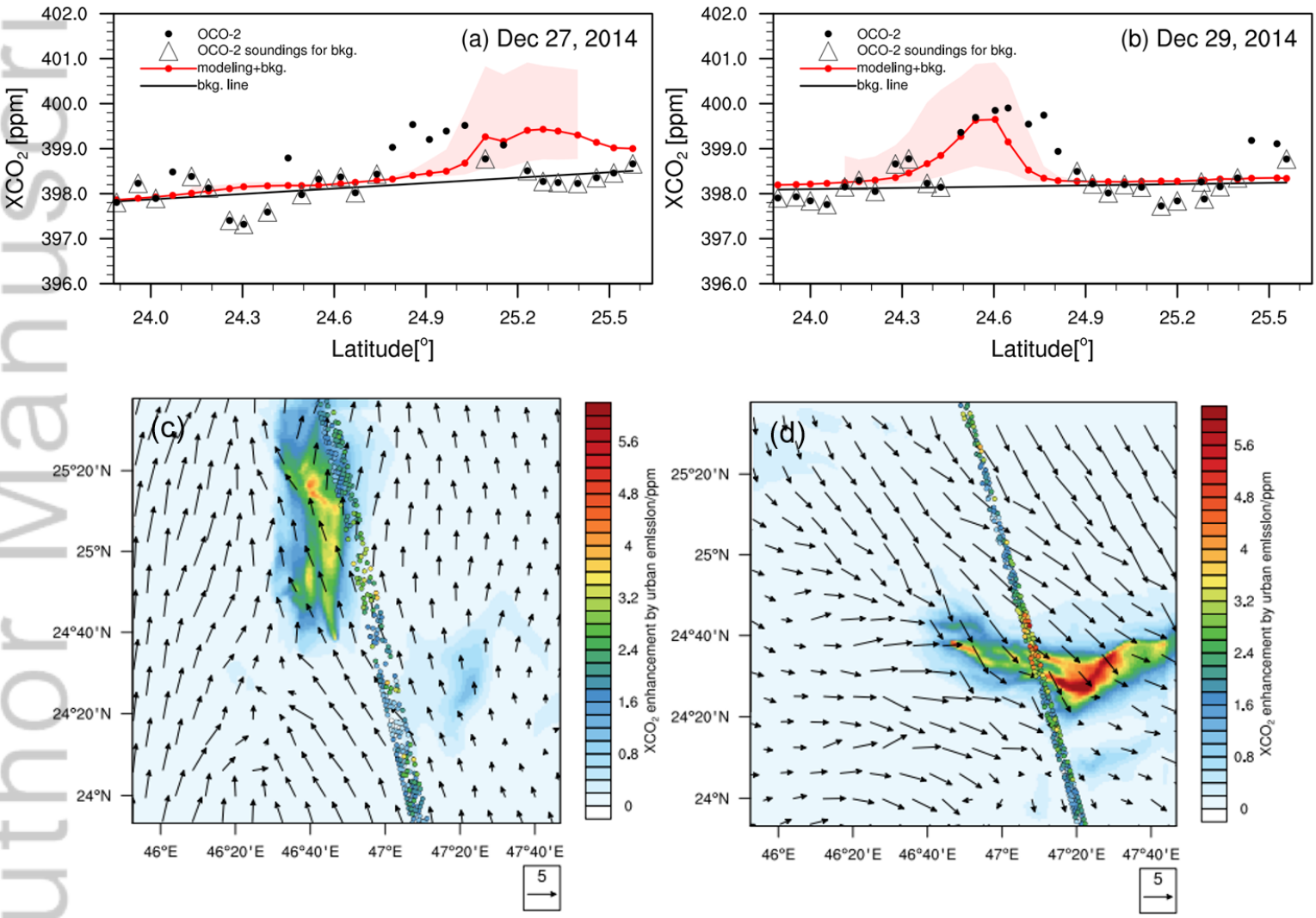

2019JD030528-f04-z-.png

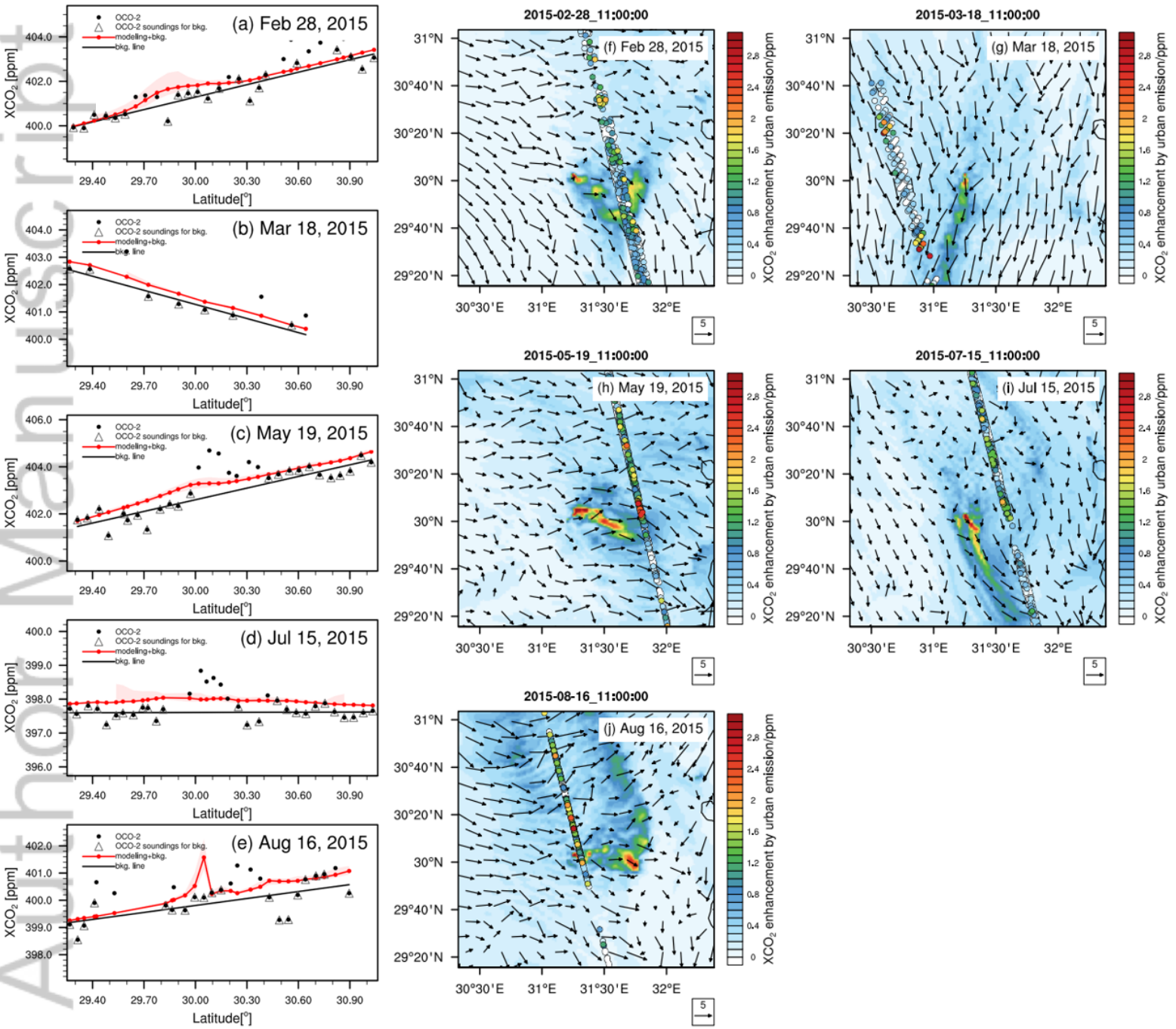

2019JD030528-f05-z-.png

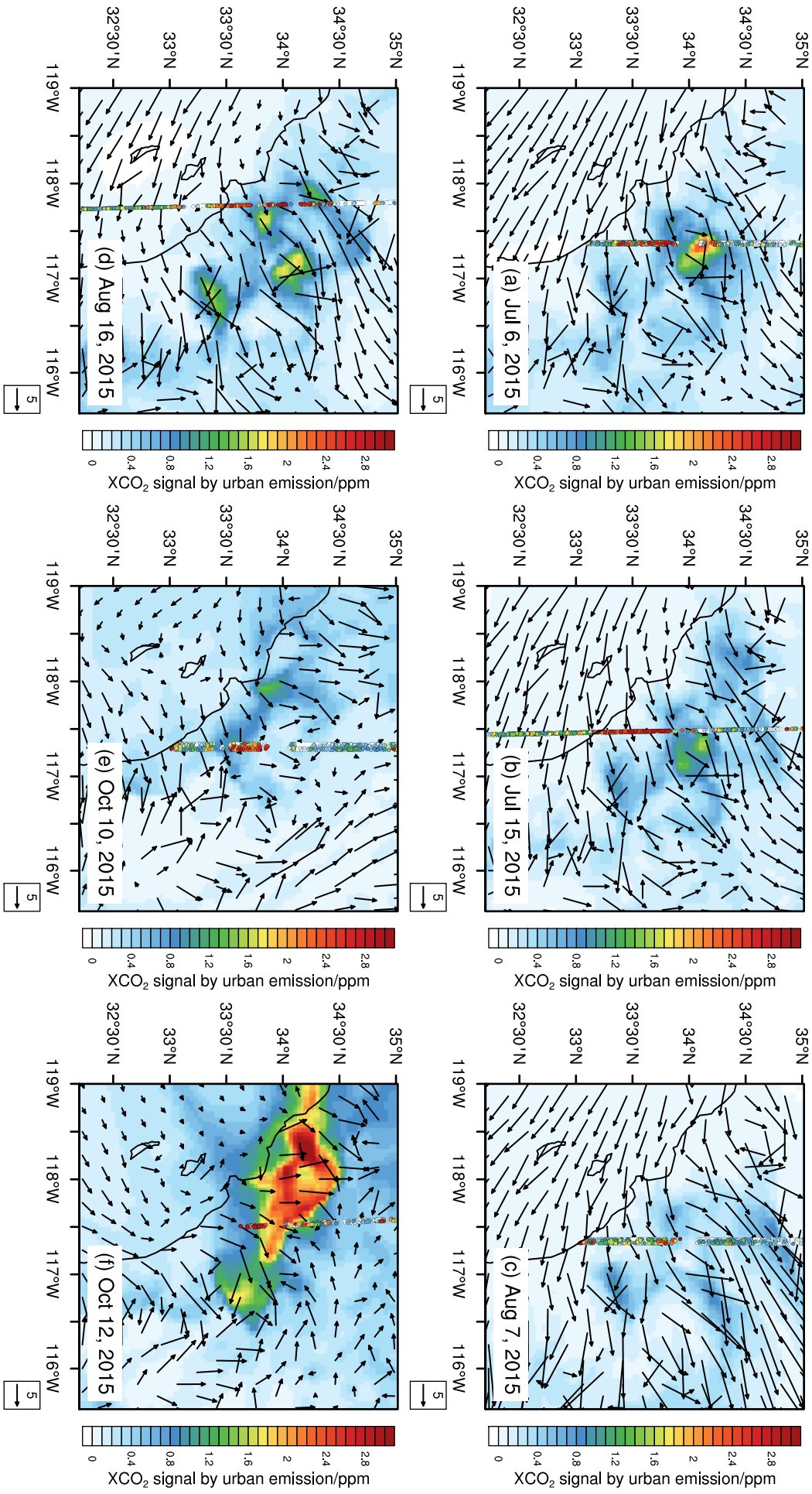

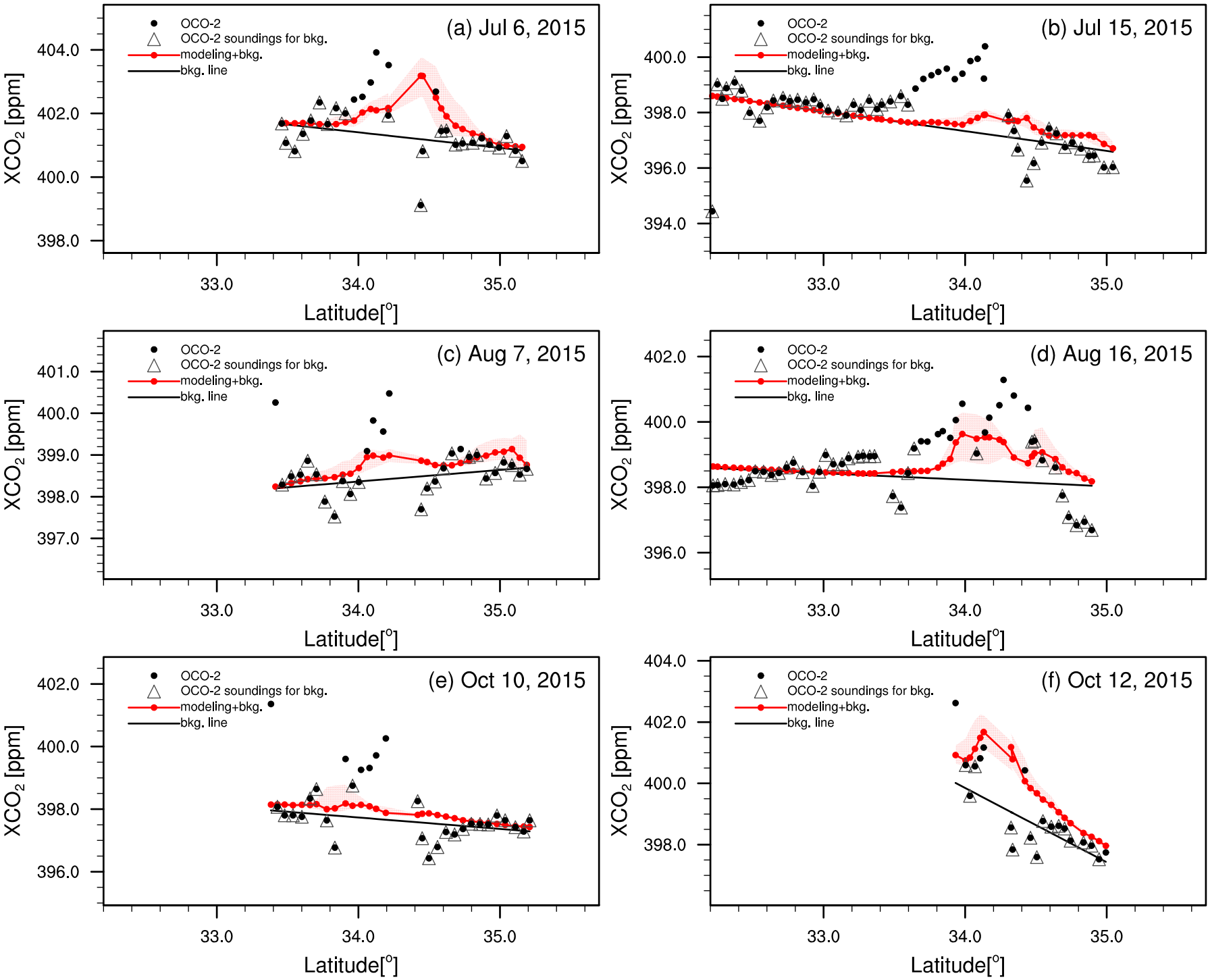

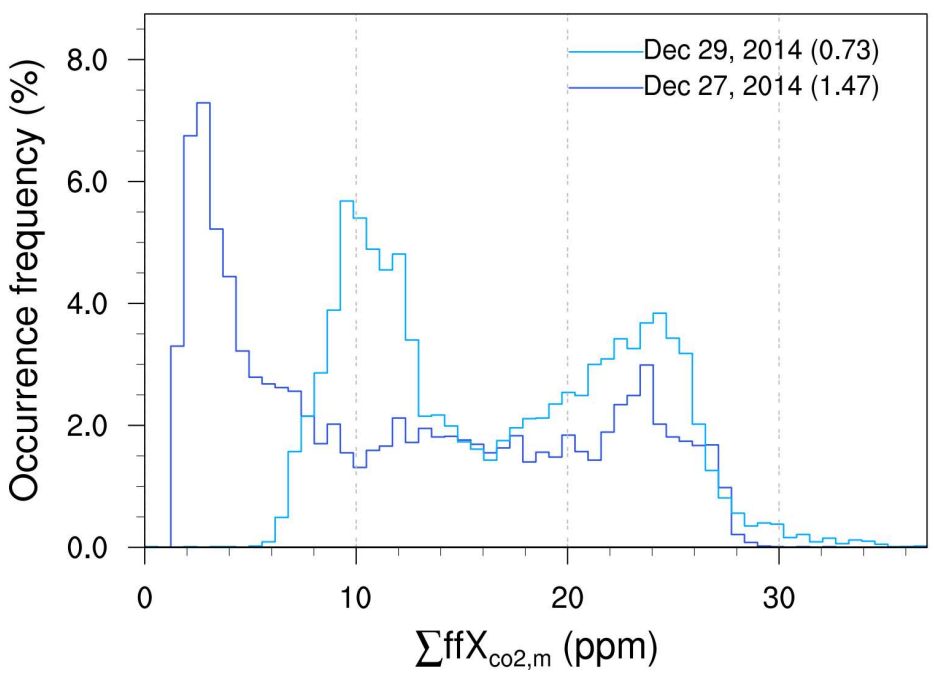

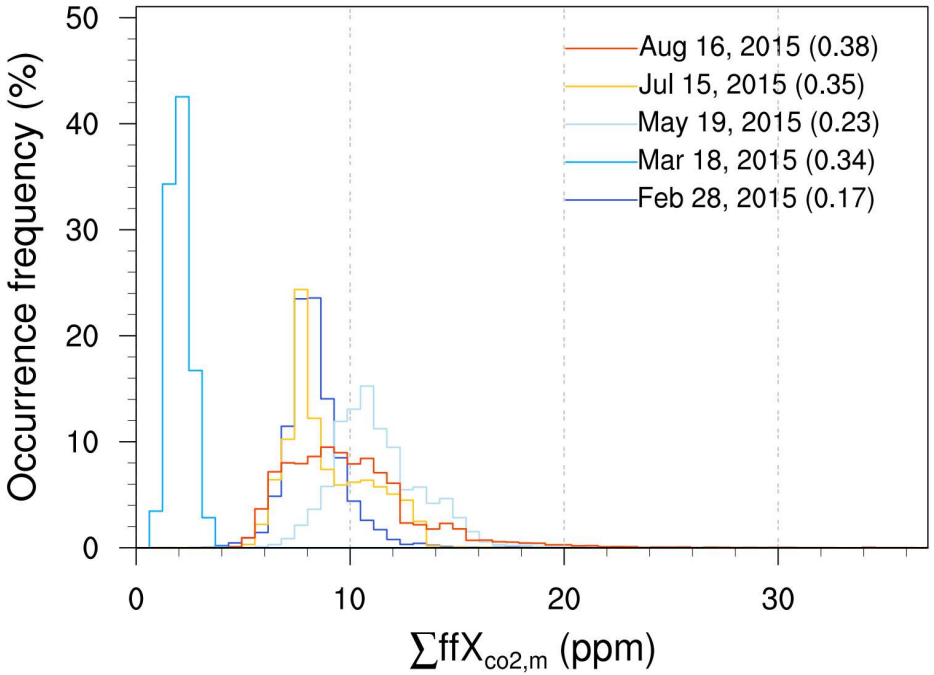

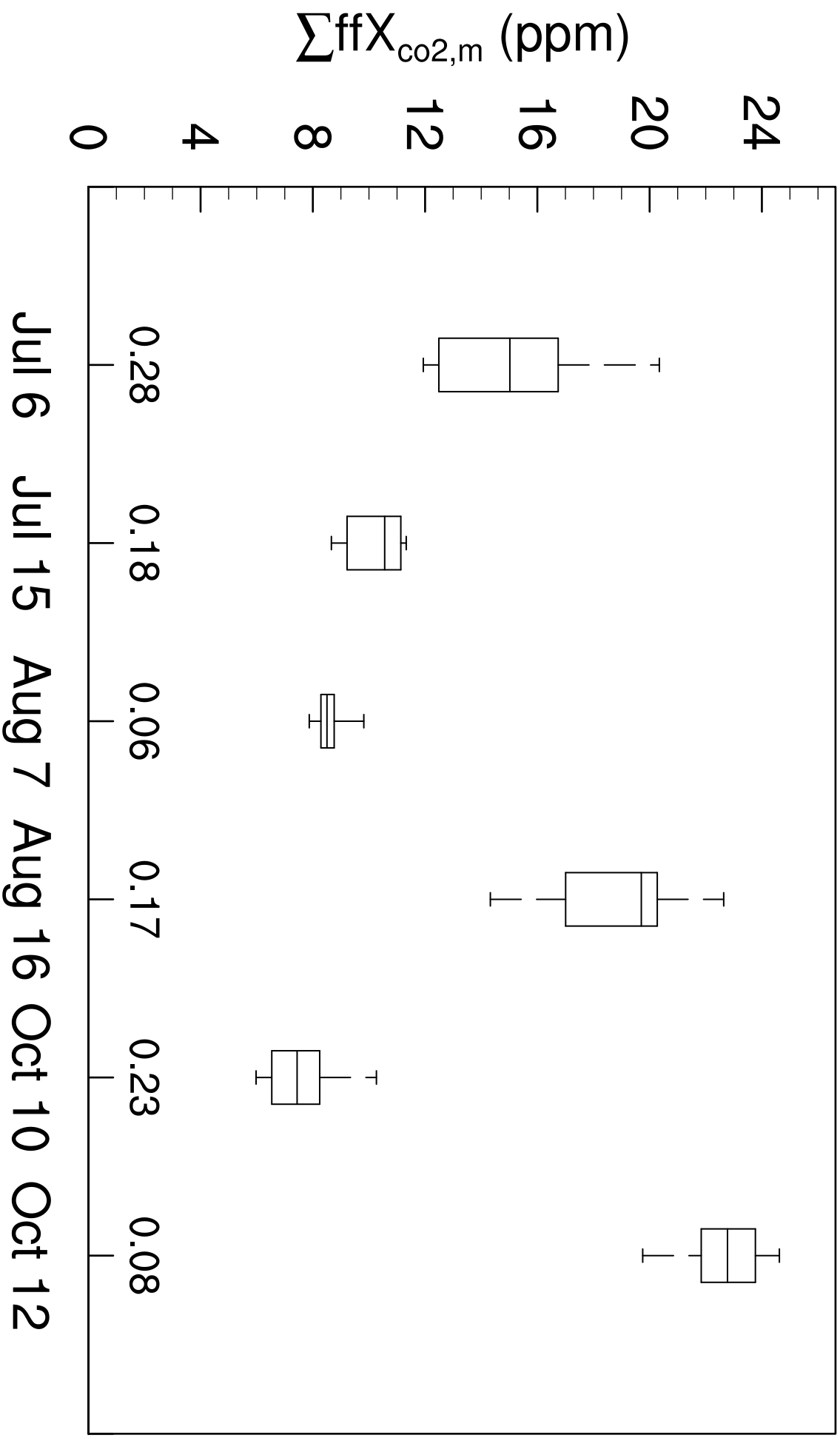

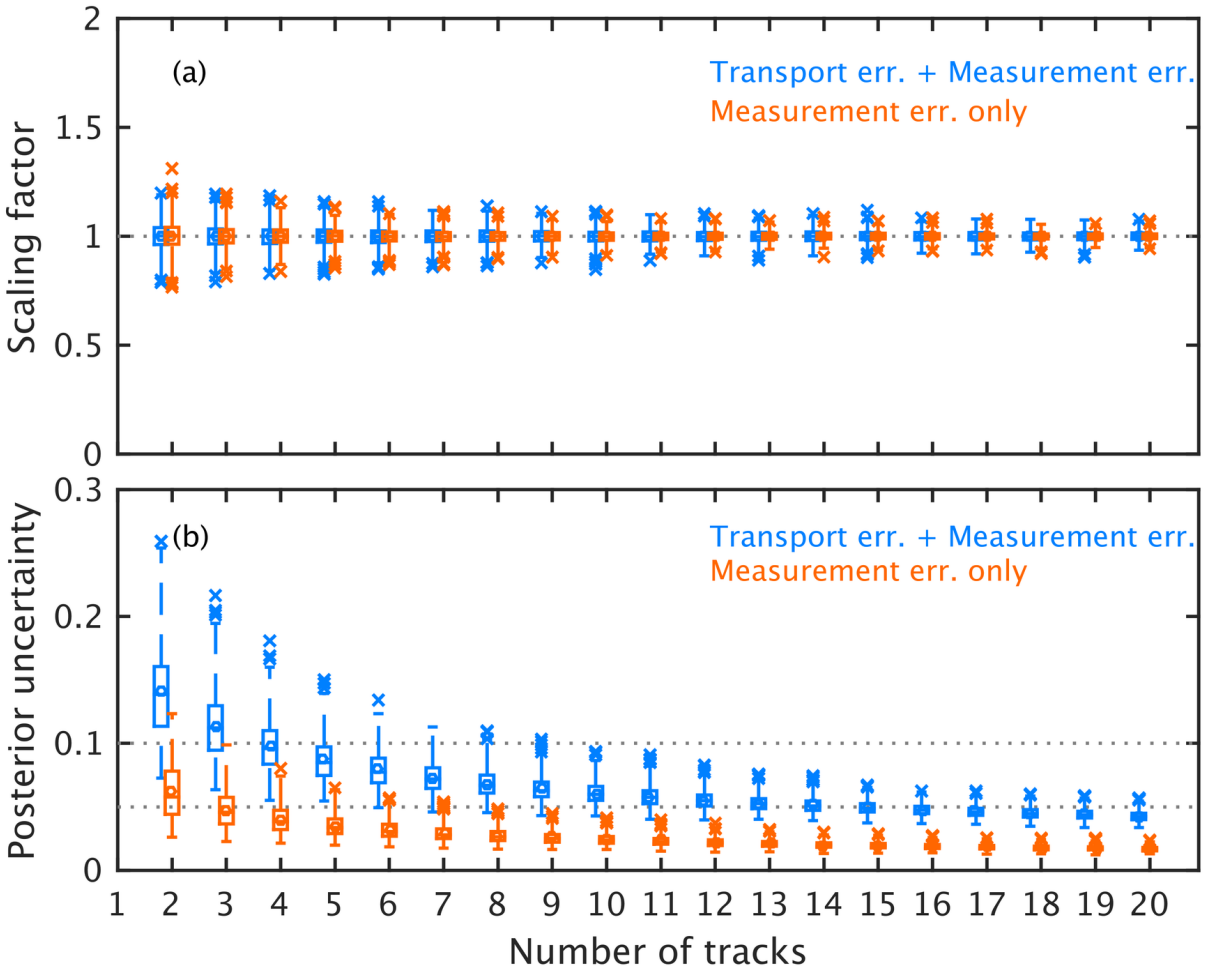

2019JD030528-f10-z-.png

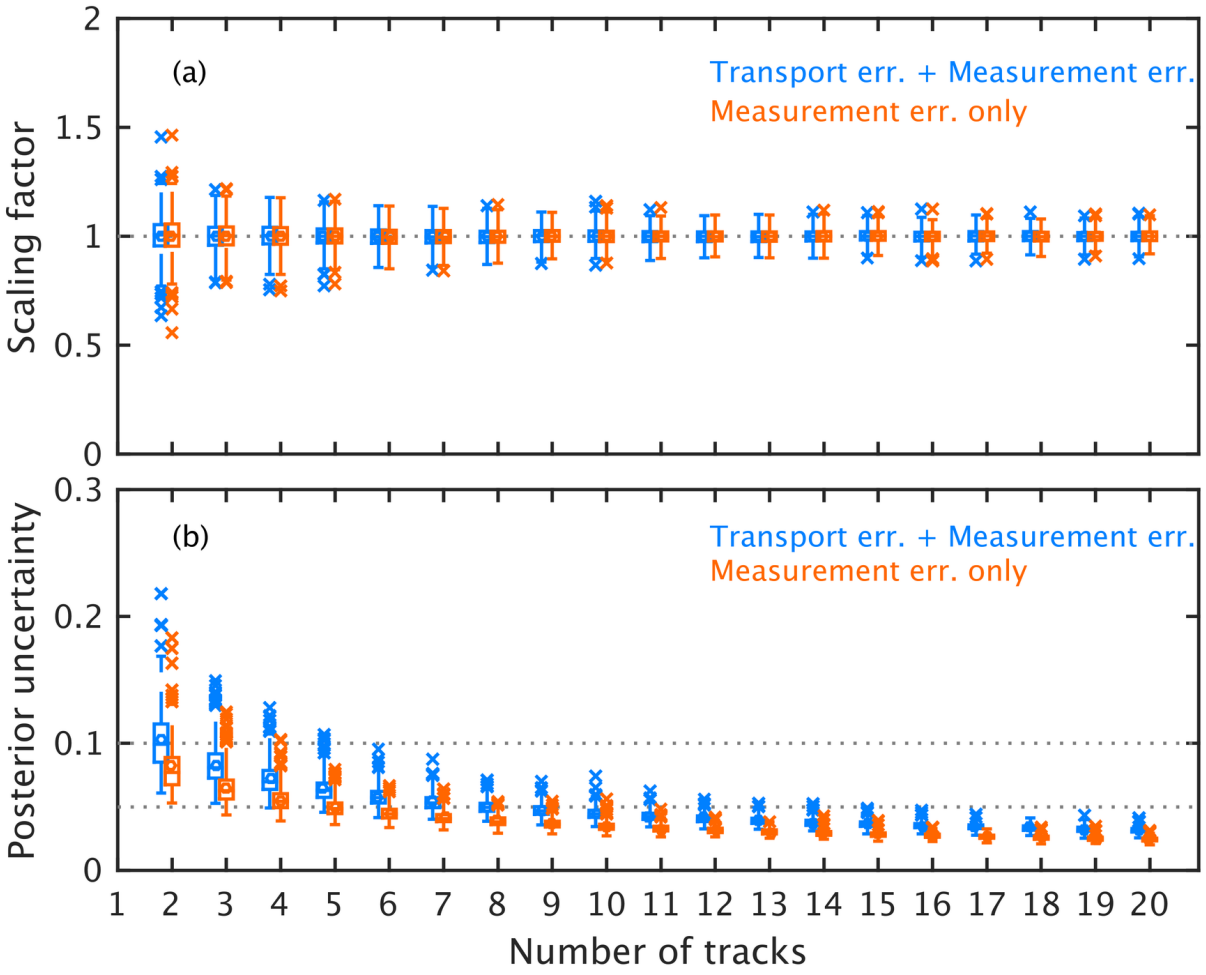

2019JD030528-f11-z-.png

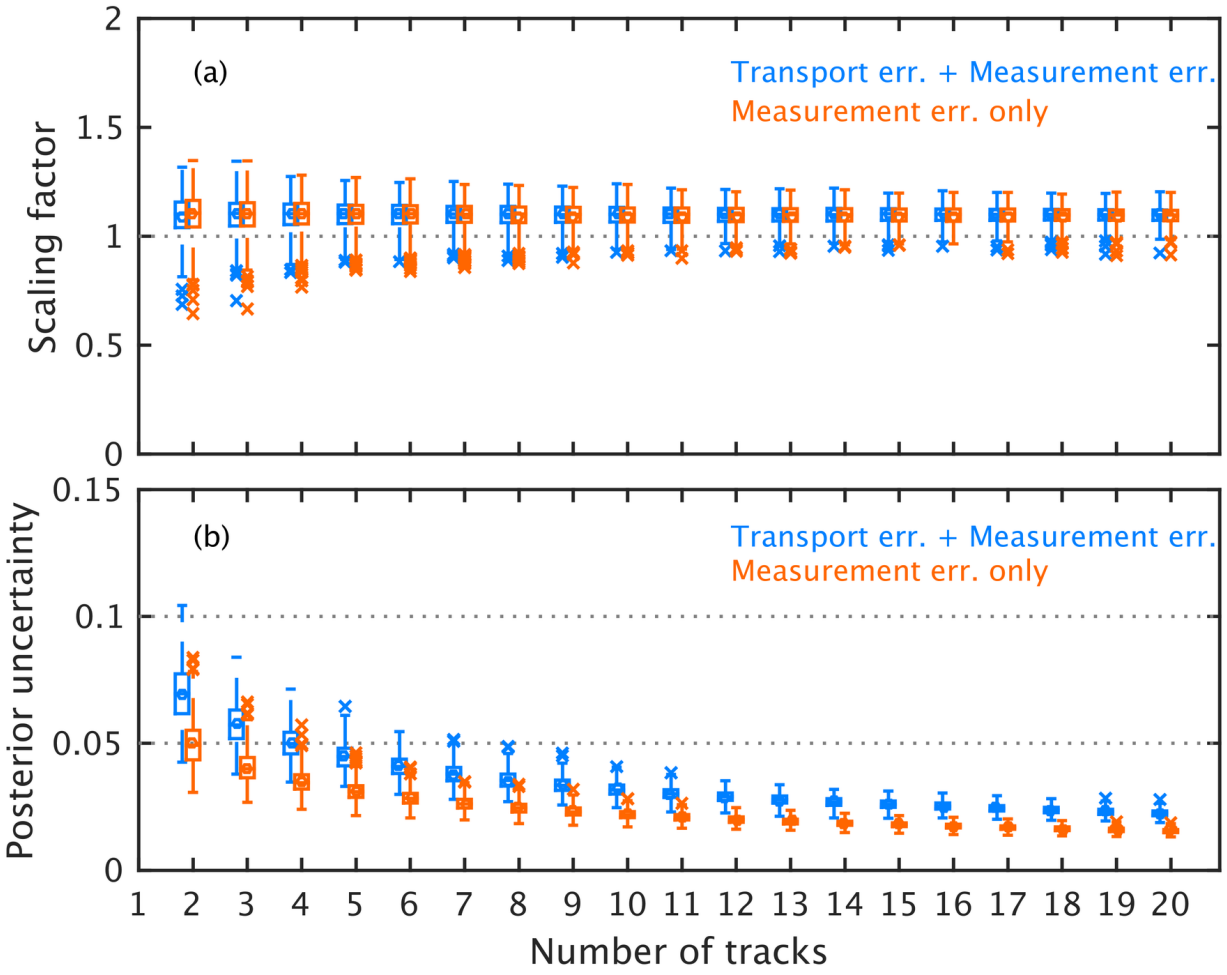

2019JD030528-f12-z-.png

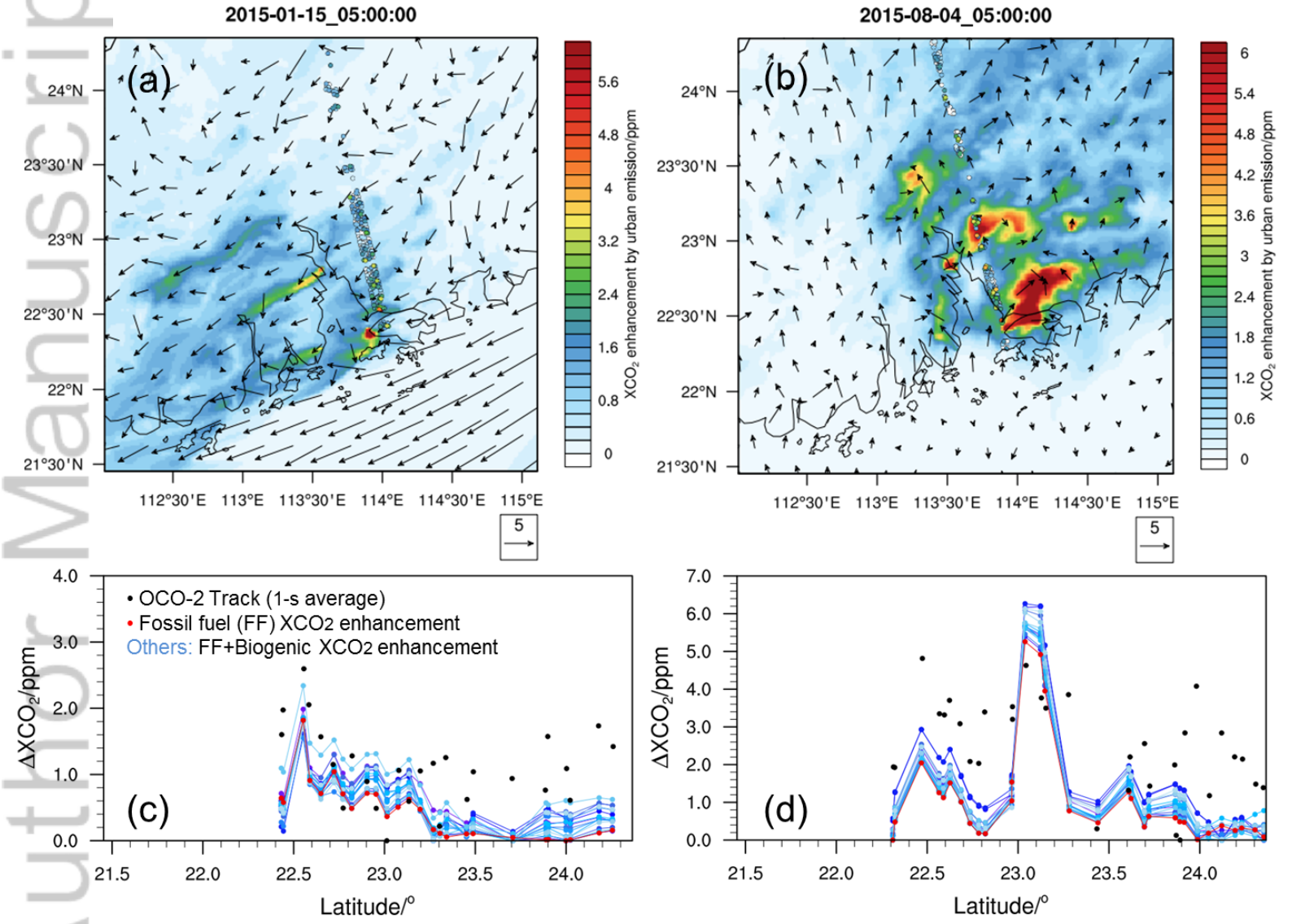

2019JD030528-f13-z-.png